PCCP

Unraveling the initial steps of the ignition chemistry of the hypergolic ionic liquid 1-ethyl-3-methylimidazolium cyanoborohydride ([EMIM][CBH]) with nitric acid (HNO_3) exploiting chirped pulse triggered droplet merging

Journal:	*Physical Chemistry Chemical Physics*
Manuscript ID	CP-ART-12-2022-005943.R1
Article Type:	Paper
Date Submitted by the Author:	03-Feb-2023
Complete List of Authors:	Biswas, Souvick; University of Hawai'i at Manoa, Department of Chemistry Antonov, Ivan; University of Hawai'i at Manoa, Department of Chemistry Fujioka, Kazuumi; University of Hawai'i at Manoa, Chemistry Rizzo, Grace ; University of Hawai'i at Manoa, Department of Chemistry Chambreau, Steven; Edwards Air Force Base, Jacobs Technology, Inc. Schneider, Stefan; Edwards Air Force Base, Air Force Research Laboratory Sun, Rui; University of Hawai'i at Manoa, Department of Chemistry Kaiser, Ralf; University of Hawai'i at Manoa, Department of Chemistry

Unraveling the initial steps of the ignition chemistry of the hypergolic ionic liquid 1-ethyl-3-methylimidazolium cyanoborohydride ([EMIM][CBH]) with nitric acid (HNO_3) exploiting chirped pulse triggered droplet merging

Souvick Biswas[a], Ivan Antonov[a], Kazuumi Fujioka[a], Grace L. Rizzo[a], Steven D. Chambreau[b], Stefan Schneider[c], Rui Sun[a*], Ralf I. Kaiser[a*]

[a] Department of Chemistry, University of Hawai'i at Manoa, Honolulu, Hawaii 96822, United States

[b] Jacobs Technology, Inc., Edwards Air Force Base, California 93524, United States

[c] Air Force Research Laboratory, Edwards Air Force Base, California 93524, United States

* Corresponding author. E-mail: ruisun@hawaii.edu; ralfk@hawaii.edu

Abstract

The composition of the products and the mechanistic routes for the reaction of the hypergolic ionic liquid (HIL) 1-ethyl-3-methylimidazolium cyanoborohydride ([EMIM][CBH]) and nitric acid (HNO_3) at various concentrations from 10 % to 70 % were explored using a contactless single droplet merging within an ultrasonic levitation setup in an inert atmosphere of argon to reveal the initial steps that cause hypergolicity. The reactions were initiated through controlled droplet-merging manipulation triggered by a frequency chirp pulse amplitude modulation. Utilizing the high-speed optical and infrared cameras surrounding the levitation process chamber, intriguing visual images unveiled: (i) extensive gas release and (ii) temperature rises of up to 435 K in the merged droplets. The gas development was validated qualitatively and quantitatively with Fourier Transform Infrared Spectroscopy (FTIR) indicating the major gas-phase products to be hydrogen cyanide (HCN) and nitrous oxide (N_2O). The merged droplet was also probed by pulsed Raman spectroscopy which deciphered features for key functional groups of the reaction products and intermediates (-BH, -BH_2, -BH_3, -NCO); reaction kinetics revealed that the reaction was initiated by the interaction of the $[CBH]^-$ anion of the HIL with the oxidizer (HNO_3) through proton transfer.

Computations indicate the formation of a van-der-Waals complex between the $[CBH]^-$ anion and HNO_3 initially, followed by proton transfer from the acid to the anion and subsequent extensive isomerization; these rearrangements were found to be essential for the formation of HCN and N_2O. The exoergicity observed during the merging process provides a molar enthalpy change up to 10 kJ mol^{-1} to the system, which could be sufficient for a significant fraction of the reactants of about 11 % to overcome the reaction barriers in the individual steps of the computationally determined minimum energy pathways.

1. Introduction

Hypergolic bipropellants are combinations of a fuel and an oxidizer that spontaneously ignite upon contact with each other.[1] Compared to the traditional non-hypergolic fuels, hypergolic bipropellants do not require an external ignition source thus reducing the design and mass of the engine. These characteristics make hypergolic propellants valuable fuel alternatives in space vehicles such as satellites and rockets.[2] Traditionally, hypergolic bipropellants have employed hydrazine (H_2NNH_2), monomethyl hydrazine [MMH, $CH_3(NH)NH_2$], or unsymmetrical dimethyl hydrazine [UDMH, $H_2NN(CH_3)_2$] as the fuel and dinitrogen tetroxide [NTO, N_2O_4] as the oxidizer.[3-5] In addition to hypergolicity, a combination of hydrazine and NTO enjoys essentials of high-performance fuels such as high energy density, low viscosity, short ignition delay (ID), and low-cost synthesis.[6-8] However, hydrazine and its derivatives along with NTO represent chemical hazards and environmental concerns: the former is highly toxic and carcinogenic, listed as "very high concern" substance as part of the REACH (registration, evaluation, authorization of chemicals) regulation,[9] while the latter has a very high vapor pressure at 300 K forming a toxic and corrosive cloud if released from its container due to leakage or spill.[10] These safety precautions involved in the handling of traditional hypergolic bipropellants impose additional high cost, thus environment-friendly high-performance hypergolic bipropellants are greatly desired.

Ionic liquids (ILs) composed of an organic cation and an inorganic or organic anion represent a low-melting - usually below 373.15 K - ionic mixture, whose intermolecular interactions are dominated by strong Coulomb interactions between the cations and the anions.[11] In 2008, Schneider *et al.*[12] reported the first hypergolic ionic liquid (HIL): an imidazolium-based cation coupled with dicyanamide anion [$^-N(CN)_2$] experienced hypergolic ignition in the presence of red-

fuming nitric acid (RFNA, ~83% HNO_3 plus 14% N_2O_4 plus ~2% H_2O plus 0.6% HF) and white fuming nitric acid (WFNA, ~100% HNO_3) as the oxidizer. In general, there are a number of factors making HILs ideal candidates for high-performance hypergolic bipropellants as compiled in the review article[13]: i) low melting point with a broad liquid range to avoid the polymorphism problem of solid fuels, ii) low viscosity to ease the supply of the fuel, iii) high thermal stability to facilitate safe handling, and iv) extremely low vapor pressure thereby lowering vapor toxicity and human exposure. These milestones intrigued numerous scientists to exploit environmentally benign energetic ILs as hypergolic bipropellants. As a result, a large number of energetic ILs have been synthesized: cations including imidazolium-based salts such as 1-butyl-3-methylimidazolium cations $[BMIM]^+$,[14] 1-ethyl-3-methylimidazolium $[EMIM]^+$,[15] triazolium-based salts like substituted 1,2,4-triazolium cations,[16] and tetrazolium-based salts, e.g., 1-amino-4,5-dimethyltetrazolium.[17] With respect to the anion, dicyanamide $[^-N(CN)_2]$ and nitrocyanamide $[^-N(NO_2)(CN)]$, which are usually paired with imidazolium cations, have attracted much attention due to its fuel-rich character as well as low viscosities, while a more recent B-H bond-rich anions such as the cyanoborohydride $[CBH]^-$ anion have shown to decrease the ignition delay (ID).[18] Nitric acid (RFNA, WFNA) and rocket-grade hydrogen peroxide (RGHP, H_2O_2 > 90%) have been considered as efficient oxidizers for its optimal fuel-performance/ environmental-impact ratio.[13]

The physicochemical properties of the HILs are essential to their application as hypergolic bipropellants. Extensive efforts have been devoted to understanding how different substituents and energy-containing groups impact these properties, including glass transition temperature, melting point, thermal decomposition temperature, density, heat of formation, predicted detonation velocity and pressure, impact and friction sensitivity, and hypergolicity (ID time).[19-24] To date, not a single HIL could meet all the essential requirements simultaneously while remaining a low-cost synthesis to replace the need of traditional hypergolic bipropellants; very often, the ID time is the most severe limiting factor.[6] ID is defined as the time that it takes to observe spontaneous ignition upon the contact between the HIL and the oxidizer. ID of less than 50 ms has been acceptable for real-life applications, although recently this goal has been shortened to 5 ms.[25] The IDs of HILs have generally been measured with a high-speed camera capturing the snapshots of dropping of HIL onto the oxidizer.[1, 26-28] The experiments have shown that although the purity of the sample, water content, and the size of the droplet impact the ID to some extent, the molecular structure of the HILs play a decisive role in the induction stage of the ignition process. The source of the ID

has been allotted to as both physical and chemical: the relatively bulkier organic cation is believed to determine the former and the relatively smaller anion is believed to determine the latter. Their relative importance varies between HILs, but the general consensus is that the hypergolicity of the HIL is determined by the *anion*.[25]

Nevertheless, a thorough understanding of the hypergolic reaction mechanism upon the contact between HILs and oxidizers plays an essential role in the designing of the next-generation HIL bipropellants. Taking the very first HIL as an example (dicyanamide-based HILs with WFNA),[12] Chambreau *et al.*[29] detected the gaseous products due to mixing of the reactants prior to the ignition event with Fourier-transform infrared spectroscopy (FTIR) to be carbon dioxide (CO_2), dinitrogen monoxide (N_2O), and isocyanic acid (HNCO), but not hydrogen cyanide (HCN); the authors interpreted their findings that the hypergolic reaction proceeds via dinitrobiuret (O_2N-NH(CO)NH(CO)NH-NO_2) and nitramide (H_2NNO_2) intermediates. This reaction was later investigated by Litzinger *et al.*,[30] who were not able to identify dinitrobiuret (O_2N-NH(CO)NH(CO)NH-NO_2), but confirmed the existence of nitramide (H_2NNO_2) as a product of the decomposition of the nitro-substituted intermediate (NC-NH(CO)NH-NO_2), which is followed by a series of protonation, nitration, and rearrangement reactions prior to ignition. Chingin *et al.*[31] utilized electrospray ionization mass spectrometry (ESI-MS) to study the ignition of dicyanamide-based HILs and reported the formation of a precipitate composed of melamine (1,3,5-triazine-2,4,6-triamine, $C_3H_6N_6$) oligomers. Their results suggest that the highly reactive intermediate like dicyanoammonia ($HN(CN)_2$) could have formed through an ion exchange between nitric acid and the IL cation. In a more recently study, Chambreau *et al.*[2] investigated the hypergolicity of dicyanamide-based HIL and nitric acid in aerosols and found a consistent mechanism as previously proposed, but argued that the diffusion within the particle may be a rate limiting step. Unfortunately, although numerous HILs have been synthesized, the investigations on their hypergolic mechanism have been very scattered and limited. In other words, chemists have learned enough about the "what" makes an IL hypergolic, but there is a certain level of lack of understanding of "why" it is hypergolic, which largely prevents them from systematically refining structure of HILs to achieve the minimal ID. The primary reason of lacking mechanistic study of the ignition of HILs is that the *in situ* generated highly energetic, reactive, and transient species in the initial stage of ignition process are very challenging to capture or probe *on line* experimentally. Further, experimental studies are conducted mainly under 'bulk' conditions with wall and surface

effects influencing the outcome of the reaction.

In recent times, computational chemistry has seen great success in guiding experimental studies in revealing such complex reaction mechanisms.[32, 33] Previous computational studies of HILs have mainly been relying on the gas-phase potential energy profile sometimes with a quantum mechanical continuum solvation model and rate constant theory to predict the mechanism of the reaction. For example, Vogelhuber *et al.*[34] investigated the oxidation of a dicyanamide-based HIL in the presence of nitric acid and argued that the inclusion of a sodium ion dramatically lowered the reaction barriers. Another branch of computational study employs molecular dynamics simulations sometimes with reactive force fields to investigate thnewnewe structure of HILs solution and molecular diffusion that contribute to the physical ID. With WFNA as the oxidizer, Sun *et al.*[27, 28] computed the radial distribution function (RDF) of a methylimidazolium cations mixed with a varying ratio of cyanoborohydride and dicyanamide anions. They concluded that 30 % of cyanoborohydride and 70 % of dicyanamide gave the shortest ID. In another study, Weismiller *et al.*[35] employed ReaxFF molecular dynamics simulations to investigate the ignition of dicyanamide-based ILs in the presence of nitric acid. By exploring two predicted intermediates, protonated dicyanamide [$HN(CN)_2$] and nitro-dicyanamide-carbonyl [$(HN)CN(CO)(NH)(NO_2)$], their results suggests that neither dicyanamide nor protonated dicyanamide are converted to 1,5-dinitrobiuret (DNB) before thermal runaway. In addition, there are also a limited number of *ab initio* dynamics simulations, also known as direct dynamics when applied to gas phase, of the HILs ignition. For example, direct dynamics trajectories of the reaction between 1-methyl-4-amino-1,2,4-triazolium [MAT^+] plus dicyanamide [DCA^-] and nitrogen dioxide (NO_2) revealed the dominant pathway to be the intra-ion-pair proton transfer between MAT^+ and DCA^-.[36] In recent times, there have been a number of computational studies involving [EMIM], notably with dicyanamide in [EMIM][DCA],[28, 36-39] as well as computational studies of HNO_3 oxidizing various ILs,[34, 40] and even CBH in a few contexts,[28, 41-43] while there has only been a single study of [EMIM][DCA] with HNO_3 as an oxidizer. Liu *et al*.[36, 37] studied [EMIM][DCA], [BMIM][DCA], and [AMIM][DCA] oxidated by NO_2. The overall reaction is broken up into two steps, a **primary** and **secondary** reaction step – the decomposition products of the former serve as reactants in the latter. According to AIMD simulations,[36, 37] [EMIM][DCA] decomposed in gas phase under high temperatures (1000-5000K) and collisions with NO_2 (0.1 eV collision energy). It is interesting that the oxidizer did not react with [EMIM][DCA], but simply acted as a source of collision energy.

After the collision, the following [EMIM][DCA] **primary** decomposition products were found: protonated $EMIM^+$ [$EMIM^+$-H^+], protonated dicyanamide [HDCA or $HN(CN)_2$], 3-methylimidazolium [MIM], ethylene [C_2H_4], ethyl cation [$C_2H_5^+$], dicyanamide [DCA^-], ethyl dicyanamide [C_2H_5DCA], and methyl dicyanamide [CH_3DCA], with the proton transfer [$EMIM^+$-H^+] being the most common (13-24% for 2000 - 5000 K). Secondary reactions of these primary products with NO_2 were done at similar conditions at two fixed collision energies (0.1 and 0.5 eV). The following **secondary** reactive (after colliding with NO_2) products were found: nitric oxide [NO], nitrous acid [HONO], hydrogen [H_2], methyl cation [CH_3^+], ethyl cation [$C_2H_5^+$], proton [H^+], nitrogen dioxide [NO_2], [O_2N-$EMIM^+$-H^+], [O-$EMIM^+$ H^+], [$EMIM^+$-H^+-H], [MIM-H], [MIM-CH_3], MIM-ONO, O-MIM, [EIM-H], [EIM-CH_3], [EIM-CH_4], [EIM-C_2H_5], 2-ethyl-1,3-imidazole, nitroethyl [$CH_2CH_2NO_2$], ethyl nitryl [CH_2CH_2ONO], and a few other short-lived species. These works are complementary with AIMD simulations of thermal excitation of [EMIM][DCA] at 4000 K.[39] The most common pathway (~ 19 out of 63 trajectories) was the proton transfer [$EMIM^+$ - H^+].

In another work, Chambreau *et al*. made brief thermodynamic arguments (M02/6-31+G(d,p) SMD-GIL condensed phase calculation) that in an oxidation of [$EMIM^+$][DCA^-] with HNO_3, the reactive species would be NO_3^- and HDCA.[38] Zhou *et al*. conducted AIMD simulations, where bimolecular reactions of DCA, HDCA, nitrate [NO_3^-], and nitric acid [HNO_3] were simulated at high temperatures (1000-5000 K) and a fixed collision energy of 0.5 eV.[40] Over 100 trajectories per reaction per temperature (1000, 2000, 3000, 4000, and 5000 K), the following products were found: nitrogen dioxide [NO_2], hydroxyl radical [OH], hydrogen isocyanide [HNC], cyanonitrene radical [NCN], and complex molecules like O_2N-$NHC(O)NCN^-$ and $HNC(-ONO_2)NCN^-$. While the most common pathway is proton transfer for both DCA+HNO_3 and HDCA+NO_3^-, formation of nitrogen dioxide [NO_2] is the most common reactive product in both cases. Further, this study looked at reactions of dicyanoborohydride (DCBH) in reaction with HNO_3, in a similar protonated/unprotonated comparison. With a similar number of trajectories (100) per reaction and temperature (3000, 4000, 5000 K for DCBH + HNO_3 and 1000, 2000, 3000K for HDCBH + NO_3^-), the following reactive products were found: hydrogen [H_2], BH_2CN, hydrogen isocyanide [HNC], hydrogen cyanide [HCN], $NCHB(-ONO_2)CN$, $NC^-(O_2NO$-HNC), and complex $HNCHBH(-ONO_2)CN^-$. While DCA and even DCBH as the anionic part have been studied, CBH has seen far less study. A summary of the potential energy profile of the anion (H_3BCN^-) and its isomer

(H_3BNC^-) has been done with a semi-empirical study[42] and the proton affinity and ionization potential of the anion have been calculated using MP2/aug-cc-pvtz//CR-CC(2)/aug-cc-pvtz.[41]

Although there are numerous experimental and computational reports on the HILs since their first synthesis, there is still an incomplete understanding of the *initial elementary steps* involved in the ignition and oxidation of HILs. An untangling of these mechanisms requires novel experimental techniques along with spectroscopic diagnostics presented here in conjunction with a computational investigation. Here, we explore both experimentally and computationally the reaction mechanisms and kinetics involved in the hypergolic reaction of droplets of 1-ethyl-3-methylimidazolium [1] $[EMIM]^+$ – cyanoborohydride [2] $[CBH]^-$ (Scheme 1) with droplets of nitric acid (HNO_3) at various concentrations from 10 % to 70 % with both reactants initially at 300 K. The experiments are conducted in an ultrasonic levitation device-[44] under container-less conditions encapsulated in a stainless-steel chamber in an argon inert gas atmosphere, in which the oxidation mechanisms of individual droplets of levitated HILs through droplet merging with the oxidizer are explored *on line* and *in situ*. The levitator incorporates complementary *in situ* diagnostics - infrared (IR), Raman (Ra), ultraviolet–visible (UV-Vis) spectroscopy, VIS/IR thermal imaging - to probe the initial oxidation processes of HILs.[25, 45-52] This is achieved by tracing the temporal evolution (kinetics) of the reactants and (functional groups of) intermediates/products formed in the oxidation processes spectroscopically and by intentionally diluting the HNO_3 reactant from WFNA down to 10 % to reduce the reactivity and to slow down the speed of the initial oxidation process thus enabling the characterizations of the initial steps of the oxidation process. This is merged with the very recent computational results on the oxidation of [EMIM][CBH] by HNO_3.[53] To our best knowledge, there has been no prior computational studies on the abovementioned system. The only computational study that involves following [EMIM][CBH] also mixes DCA and AMIM as the ionic liquids, which are oxidized by HNO_3, and the focus of the study was to understand their viscosities, densities, decomposition temperatures, and specific impulses.[28] The computational method employed was classical molecular dynamics without any *ab initio* calculation, thus it was unable to predict accurately the underlying reaction mechanism of the system.

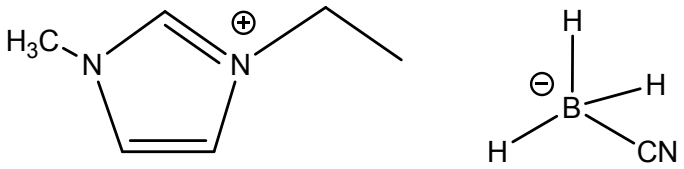

EMIM
[1]

CBH
[2]

Scheme 1. Structure of 1-ethyl-3-methylimidazolium [1] $[EMIM]^+$- cyanoborohydride [2] $[CBH]^-$.

2. Experimental Technique

2.1. Ultrasonic levitator apparatus. The levitator apparatus (Figure 1) used in the present experiment has been discussed in detail previously.[25, 45-52, 54] Briefly, in this acoustic levitator, ultrasonic sound waves with a frequency of 58 kHz are produced by a piezoelectric transducer and they get reflected from a concave plate mounted vertically upwards thus generating a standing wave.[44] The soundwaves produce acoustic radiation pressure, which allows a liquid droplet or a tiny solid particle to levitate slightly below one of the pressure minima of the standing wave.

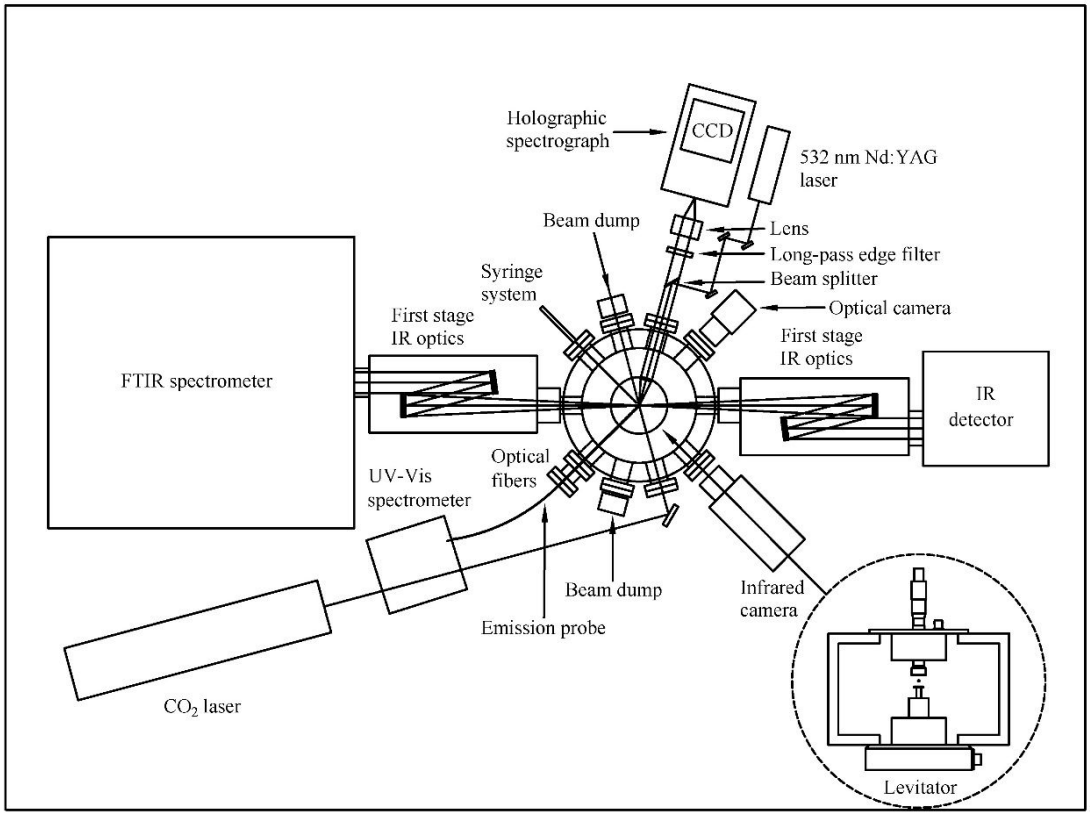

Figure 1. Schematic top view of the complete levitator apparatus displaying the ultrasonic levitator, process chamber, carbon dioxide laser, Raman spectrometer, FTIR spectrometer, fiber optic UV-vis spectrometer, infrared camera, and optical camera.

The distance between the transducer and reflector is set to 2.5 times the wavelength of the soundwave used in the set up (or 14.8 mm) producing five pressure nodes in total, although only the second and third pressure nodes above the ultrasonic transducer are suitable for levitation. The largest diameter of droplets or particles that can be held steadily while levitated in the present apparatus is approximately 3 mm, whereas the smallest could be as low as 15 μm. In this work, the droplets loaded in the pressure nodes before merging were oblate spheroidal shaped and their horizontal and vertical diameters measured in the ranges of 1.8-3.0 mm and 1.0-2.1 mm, respectively. The volumes of the droplets were also calculated and provided in Table S1.

2.2. The process chamber and sampling system. The levitator assembly is enclosed within a pressure-compatible process chamber (Figure S1) with a total volume of about 15 liters made of stainless steel to permit levitation in an inert gas or a highly reactive gas to investigate chemical reactions. In the present experiments, the chamber was filled with argon at the temperature and pressure of 298 K and 900 Torr, respectively. To load chemically distinct droplets in adjacent pressure nodes of the levitator, two syringes are attached to an outside port on the chamber. Each syringe is connected via chemically inert teflon tubing to one of two microneedles inside the chamber. The pair of needles is attached to the end of a wobble stick. This dual droplet deposition system enables either needle tip to be precisely positioned within the second or third pressure minimum to load a droplet before being withdrawn to a rest position prior to the experiments.

2.3. Droplet merging. The principle of droplet merging relies on the induction of new oscillations to either of the droplets or both.[25] The oscillations are generated by the amplitude modulation using a low-frequency voltage output from a signal generator (Keysight 10 MHz Function/Arbitrary Waveform Generator-33210A). The voltage V_a applied to the ultrasonic transducer is given by-

$$V_a = V_c(1 + m\sin\omega_m t)\sin\omega_c t \quad (1)$$

where V_c and ω_c are the voltage amplitude and angular frequency ($\omega_c/2\pi$ = 58 kHz) of the unmodulated ultrasonic standing wave, respectively; ω_m is the angular frequency of the modulation voltage with typical values in the range of $1 \lesssim \omega_m/2\pi \lesssim 50$ Hz; and m is the modulation index. The radiation pressure is proportional to the time average of the acoustic pressure amplitude of the standing wave squared. The force acting on a droplet in the absence of modulation is due to two main sources - radiation pressure of the standing wave and gravity. At the equilibrium trapping position slightly below the pressure node the upward vertical acoustic pressure force completely compensates the downward gravitational force (the net force is zero) and the droplet levitates. When the amplitude modulation is applied, the acoustic force changes with time while the gravity is constant; thus the net force oscillates. This oscillation results in exciting of vertical oscillations of the droplet out of the equilibrium position along with simultaneous deformation from oblate to prolate spheroid. The oscillations rapidly increase with time if the applied amplitude modulation frequency (ω_m) matches the resonant frequency of the droplet determined by the curvature of the trapping potential which in turn depends on the droplet size, mass and acoustic pressure. Thus, relatively small amplitude modulation ($m<<1$) can result in high amplitude vertical oscillations of the droplet causing it to leave a pressure node and subsequently merge with a droplet in a different pressure node. A brief description about the generation of merging motion of the approaching droplet induced by the amplitude modulation has been provided in the Supplementary Information, S1. Here, the surface tension of the droplets act as a restoring force during the merging event. As the best modulation frequency for droplet merging depends on the chemical and physical properties of the droplets, pressure in the process chamber and various other parameters; it requires extensive 'trial-and-error' experiments. In case of experiments with corrosive chemicals, this is not desirable. Therefore, instead of working at a fixed modulation frequency, a chirped pulse was applied. In brief, a chirp of frequency range 1 Hz to 50 Hz was utilized to automatically find the best modulation frequency for droplet merging; as a positive side effect, this increases the success of droplet merging to nearly 100 %. The key steps to achieve merging of the droplets is depicted in Figure 2 and the detailed description can be found in the Supplementary Information, S2.

The droplet merging and the successive physical and chemical changes due to this event occur at a few milliseconds time regime; therefore, spectroscopic as well as visual detection methods needed to be synchronized. For this purpose, all of the data collection tools except the FTIR spectrometer were synchronized and externally triggered by a pulse generator, (Quantum

Composer Plus, model-9518) operating at 1 kHz repetition rate. The typical pulse sequencing used is described in Supplementary Information S3 and Figure S2.

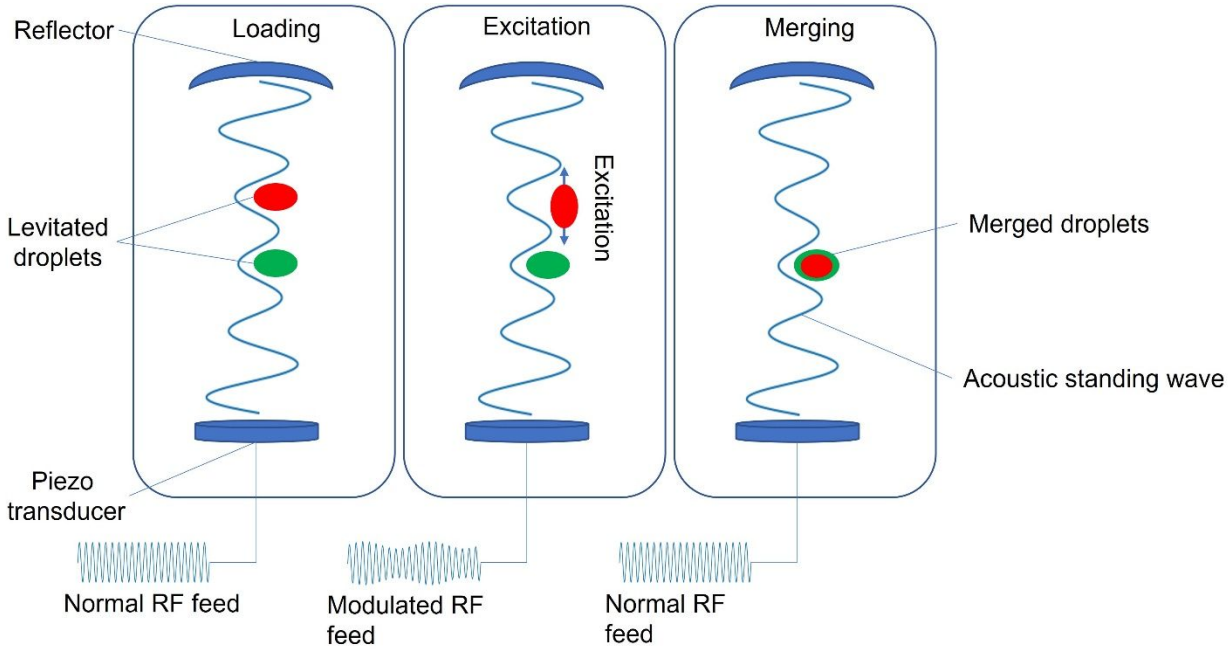

Figure 2. Schematic of droplet merging approach in the ultrasonic levitator utilizing a chirped pulse to match the modulation frequency.

2.4. Spectroscopy. The process chamber is surrounded by complementary FTIR and Raman spectrometers to identify any characteristic chemical or physical alterations of the levitated sample. There is also a UV-vis probe (StellarNet SILVER-Nova, spectral resolution = 2 nm) which is capable of measuring emission spectral traces resulting from ignition in a millisecond temporal resolution.

2.4.1. Raman spectroscopy. In the Raman spectrometer system, the allowed vibrational transitions were excited by the 532 nm line of a diode-pumped, Q-switched Nd:YAG laser (CrystaLaser, model QL532-1W0) having a beam diameter of 0.35 mm and a divergence angle of 3.8 mR. The average power output from the laser was about 200 mW and its pulse width was 13.5 ns operating at 1 kHz repetition rate. The laser beam was introduced into the chamber through an antireflection coated window from a mirror (Edmund Optics, model NT45-991, >99% reflectance) followed by a dichroic beam splitter (Semrock, RazorEdge, model LPD01-532RU-25 × 36 × 2.0).

A plano-convex lens with a focal length of 60 mm focused the laser beam onto the sample to form a spot with a diameter ($1/e^2$) of approximately 20 μm. The Raman-shifted photons, backscattered from the droplet are then passed through an ultra-steep long-pass edge filter (Semrock, model LP03-532RE-25) which cuts down the elastically scattered 532 nm laser light. Further the resultant backscattered photons were focused by a 50 mm f/1.8 camera lens (Nikon, Nikkor 2137) into a HoloSpec f/1.8 holographic imaging spectrograph (Kaiser Optical Systems, model 2004500-501 and Holoplex HPG-532) equipped with a PI-Max 2 ICCD camera (Princeton Instruments) through a slit (width = 100 μm). The CCD detector is composed of 1024 × 256 pixels each having a spatial resolution of 26 μm. The spectra were collected over the Raman-shift ranges of 200-2450 cm^{-1} and 2400-4000 cm^{-1} simultaneously which are obtained by dispersing the total signal by the two overlaid holographic transmission gratings. The resolution of the Raman spectrometer is 9 cm^{-1}. Both the excitation laser and the detector are operated at 1 kHz repetition rate and they are externally triggered and synchronized via a pulse generator, Quantum Composer Plus, model-9518. In order to accumulate only Raman scattering signal, the pulse width for the ICCD detector is kept typically around 50 ns and accumulation time for each spectral trace was kept in the range of 10-50 seconds. For the experiments presented here a typical gate delay in the range of 480-500 ns was used and gates per exposure was fixed at 1000 shots. For the ionic liquid sample, background fluorescence was observed in the Raman spectral traces. In order to suppress the fluorescence, a pre-treatment of photoprocessing for the sample was performed. The photoprocessing was essentially the exposure of the levitating ionic liquid droplet with a loosely focused (about 2 mm beam diameter) 532 nm laser at 200 mW until the point where the fluorescence background in the Raman spectrum had completely diminished. As verified by FTIR and Raman scans, this treatment did not destroy or chemically modify the ionic liquid. The Raman spectrometer was calibrated, i.e. pixel versus wavenumber by recording Raman spectra for levitating droplets of cyclohexane (C_6H_{12}), toluene ($C_6H_5CH_3$) and acetonitrile (CH_3CN).

2.4.2. FTIR spectroscopy. The gases produced by the merging of the droplets were identified by collecting an FTIR transmission spectrum in the 400-4000 cm^{-1} wavenumber region through the full width of the process chamber. The FTIR spectrometer system combines a Nicolet 6700 FTIR spectrometer (Thermo Scientific) with two stages of copper mirror optics. The infrared incident beam from the spectrometer was focused into a diameter of 4 mm around the levitated sample before re-collimating prior to detection by a liquid nitrogen cooled MCT-B (mercury cadmium

telluride, wide band) detector. The FTIR spectrum of the ionic liquid [EMIM][CBH] was recorded by preparing a thin film ex-situ. The acquisition time for each spectrum was 15 s at a spectral resolution of is 4 cm^{-1} for the instrument. In the experiment, the data acquisition of the gaseous products generated was initiated immediately after loading the droplets; the data collection operated during the merging and also after the merging event while the merged droplet was still levitating to observe the production of gaseous products. The background infrared spectrum was recorded each time before loading the droplets, only with argon in the process chamber. The number densities or number of moles of the gases (for hydrogen cyanide (HCN), nitrous oxide (N_2O), nitrogen dioxide (NO_2), and nitric oxide (NO)) evolved during merging events followed by droplet merging and hence chemical reactions were evaluated directly from the calibration curves obtained by taking different pressures of the respective gases individually in the process chamber maintaining the identical experimental conditions (Supplementary Information S4, Figures S3-S6).

2.5. The optical and infrared movies and snapshots. To record high-speed events, a Phantom Miro 3a10 camera operating at repetition rate up to 1 kHz combined with a Navitar Zoom 6000 modular lens system was aligned on the levitated sample via an optical viewport. Infrared thermal imaging videos of the merging events were recorded using an FLIR A6703sc camera. The camera was set to a repetition rate of 250 Hz and the infrared camera was also used to determine temperature changes of the levitated droplets as well as the merged droplet. Both of the optical and IR camera were triggered externally by the pulse generator synchronized with the Raman spectrometer.

2.7. Chemicals and gases. The sample 1-ethyl-3-methylimidazolium cyanoborohydride (Scheme 1) was synthesized in house.[15] Concentrated nitric acid (HNO_3,70%) and hydrochloric acid (HCl) were procured from Sigma Aldrich and Fisher Chemicals, respectively. The dilution of the acids was carried out by using HPLC grade water (Sigma Aldrich). Argon (99.9999%, Ar) gas to fill the levitator process chamber was procured from Airgas. The gases for the calibration purposes were supplied by Matheson Tri-gas: hydrogen cyanide (HCN, diluted 5% in helium), nitrous oxide (N_2O, purity: 99.999%), nitric oxide (NO, diluted 1% in argon), nitrogen dioxide (NO_2, diluted 0.5% in argon).

3. Results and discussion

3.1. Characterizations of the reactants

3.1.1. Raman spectra of the ionic liquid ([EMIM][CBH])

In order to accurately identify and to assign newly emerging features during the reaction of the ionic liquid with the oxidizer, it is important to first tabulate the absorptions of the reactants. A Raman spectrum of the levitating droplet of the unreacted ionic liquid [EMIM][CBH] in the argon atmosphere inside the levitator process chamber is depicted in Figure 3. The Raman spectrum was deconvoluted to identify individual peaks and the optimized peak wavenumbers are compiled in Table 1 along with their assignments.

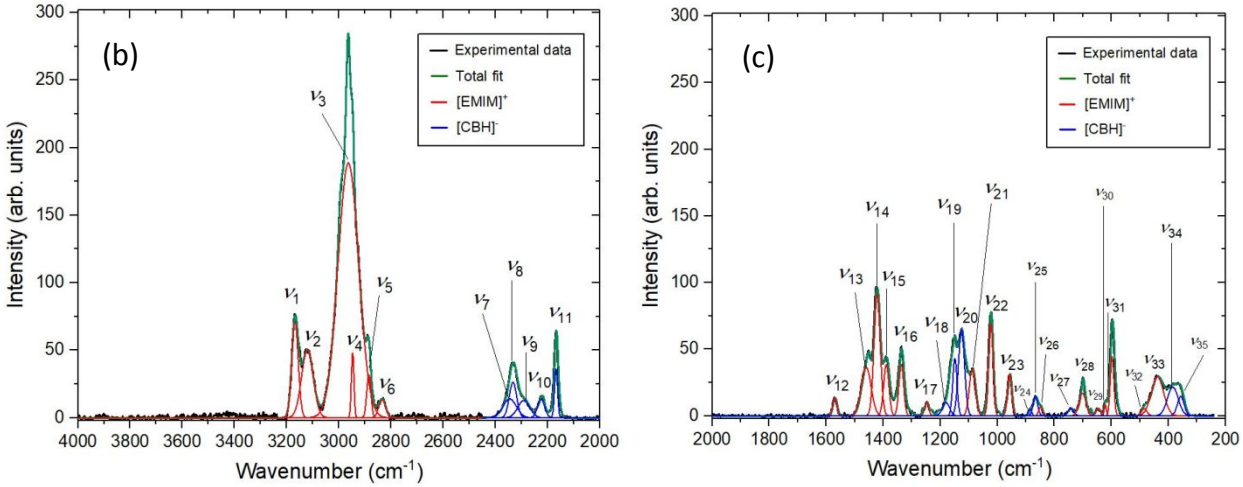

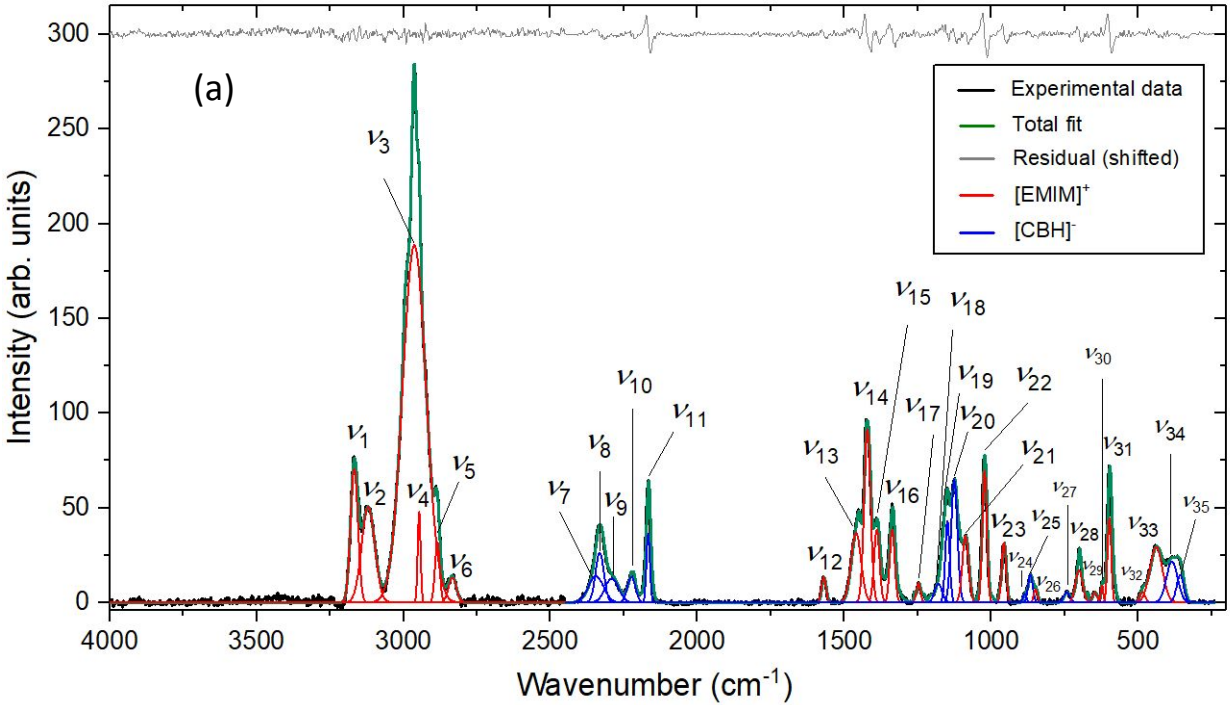

Figure 3. Raman spectrum with deconvolution for the hypergolic ionic liquid [EMIM][CBH]; - (a) full range (4000-200 cm^{-1}), (b) 4000-2000 cm^{-1} and (c) 2000-200 cm^{-1}.

Table 1: Assignment of the bands/peaks in the Raman spectrum for the hypergolic ionic liquid [EMIM][CBH].[55-57]

Band	Vibrational mode description	Measured wavenumber (cm^{-1}) (this work)	Literature wavenumber (cm^{-1}), intensity
ν_1	ν (aro C-H)	3168	3172, w
ν_2	ν (aro C-H)	3121	3122, vw
ν_3	ν_{as} CH_3, CH_2	2964	2971, s
ν_4	ν_{as} CH_3 (Et)	2948	2964, m
ν_5	ν_s CH_3 (Et)	2887	2887, w
ν_6	ν (ali C-H)	2834	2839, vw
ν_7	ν_e (B-H)	2348	2350, m
ν_8	ν_e (B-H)	2332	2334, s
ν_9	ν^{a1} (B-H)	2285	2280, sh
ν_{10}	ν^{a1} (B-H)	2223	2239, m
ν_{11}	ν^{a1} (C≡N)	2169	2177, vs
ν_{12}	ν (C=C), ν_{as}(ring)	1569	1567, w
ν_{13}	δ_{as} CH_3 (Me)	1455	1456, m
ν_{14}	δ_s CH_3	1423	1418, s
ν_{15}	δ_s CH_3 (Et), w CH_2	1390	1381, m
ν_{16}	ν N-Et, N-Me, breathing	1337	1334, s
ν_{17}	*r* (aro C-H)	1247	1257, w

ν_{18}	δ^{e} (B-H)	1184	1195, m
ν_{19}	δ^{a1} (B-H)	1148	1136, sh
ν_{20}	δ^{a1} (B-H)	1124	1123, m
ν_{21}	*r* (ring C-H), *r* (ali)	1089	1092, m
ν_{22}	δ (ring), breathing, ν (C_{ali}-N)	1024	1026, m
ν_{23}	γ (aro C-H)	957	962, w
ν_{24}	r^{e} (B-H)	886	888, vw
ν_{25}	ν^{a1} (B-C)	866	870, vw
ν_{26}	γ (C-H)	848	829, vw
ν_{27}	ν^{a1}BN ($BH_3CNBH_3^-$ isomer)	742	742, w
ν_{28}	ν (C_{ali}-N)	702	701, m
ν_{29}	γ N-Et, γ N-Me	648	649, vw
ν_{30}	γ N-Me	622	624, w
ν_{31}	ν N-Et, ν N-Me	597	599, vs
ν_{32}	-	487	-
ν_{33}	*r* N-Et, *r* N-Me	439	438, m
ν_{34}	δ^{e} (BCN)	384	358, vw
ν_{35}		358	

Abbreviations used: vw, very weak; w, weak; m, medium; s, strong; vs, very strong; sh, shoulder; ν_s, symmetric stretch; ν_{as}, asymmetric stretch; ν (X-Y), stretch between X and Y atoms; v_i, indexed bands from the Raman spectrum in Figure 3; δ, bend; *w*, wagging; *r*, rocking; γ, out of plane; aro, aromatic; ali, aliphatic; *e*, approximated band assignments in the literature [Ref. 55-57]

The bands were color coded to distinguish the cation ($[EMIM]^+$) and anion ($[CBH]^-$) of the ionic liquid. To our best knowledge, a detailed spectroscopic study on [EMIM] [CBH] has been lacking prior to this work. Therefore, the vibrational modes for this ionic liquid were assigned by comparing the best-fit peak wavenumbers with experimentally measured and theoretical values for ionic liquids containing the individual cation and anion. For example, the assignments for the cationic part ($[EMIM]^+$) were adopted from Katsyuba *et al*.[56, 57] The most intense feature in the spectrum labeled ν_3 (2964 cm^{-1}) corresponds to the asymmetric stretch of the CH_2 moiety in the aliphatic side chains of the $-CH_3$ or $-CH_3CH_2$ groups attached to the imidazolium ring. Characteristic aromatic C-H stretching frequencies (ν_1 and ν_2) are noted within the region of 3180-3120 cm^{-1}. The bending vibrations of the aliphatic hydrocarbon chain (ν_{13}, ν_{14} and ν_{15}) appear prominently in the 1500-1350 cm^{-1} segment of the spectrum. The band at 1569 cm^{-1} (ν_{12}) is linked to the aromatic C═C stretching mode of the imidazolium ring; characteristic vibrational modes corresponding to N-aliphatic chain linkages were located at 1337 cm^{-1} (ν_{16}). Below 1100 cm^{-1}, the spectral trace contains bands originating from the bending vibrations and deformations of the aromatic imidazolium moiety. A set of bands between 2450 and 2100 cm^{-1} can be linked to the signatures of the CBH anion. Due to the scarcity of Raman and infrared spectroscopic data for the

CBH^- in an ionic liquid, we exploited the study of $[BH_3CN]^-$ from the corresponding potassium and sodium salts reported by Berschied et al.[55] for detailed vibrational mode assignments. The peaks ν_7 to ν_{10} can be exclusively assigned to B-H stretching vibrations for the groups BH and BH_2, in which the hydrogen atom is free or often termed as 'terminal hydrogens' in the literature. The existence of the -C≡N functional group has been confirmed from the sharp and strong transition at 2169 cm^{-1} (ν_{11}). A set of congested bands (ν_{18}, ν_{19}, ν_{20}) obtained after deconvolution are assigned to the bending modes of the $–BH_2$ moiety at 1184, 1148 and 1124 cm^{-1}, respectively. The B-C stretching vibration in the anion appears as a weak feature at 866 cm^{-1} (ν_{25}). A very weak band (ν_{27}) at 742 cm^{-1} is assigned to the BN stretching mode of the $BH_3CNBH_3^-$ isomer. The negligible intensity of the peak ensures that the ionic liquid does not undergo oligomerization, hence maintaining the optimum reactivity for a longer duration. In the low frequency region, the BCN bending vibrations were identified in the Raman spectrum at 384 and 358 cm^{-1} (ν_{34} and ν_{35}).

3.1.2. FTIR spectra of the ionic liquid ([EMIM][CBH])

An FTIR spectrum of a thin film of the ionic liquid [EMIM][CBH] is shown in Figure 4 along with the spectral deconvolution. Similar to the Raman spectrum, the features are color coded in red for $[EMIM]^+$ and blue for the $[CBH]^-$. The optimized band positions obtained by peak fitting are listed in Table 2 with their assignments compared with prior literature.[55-57]

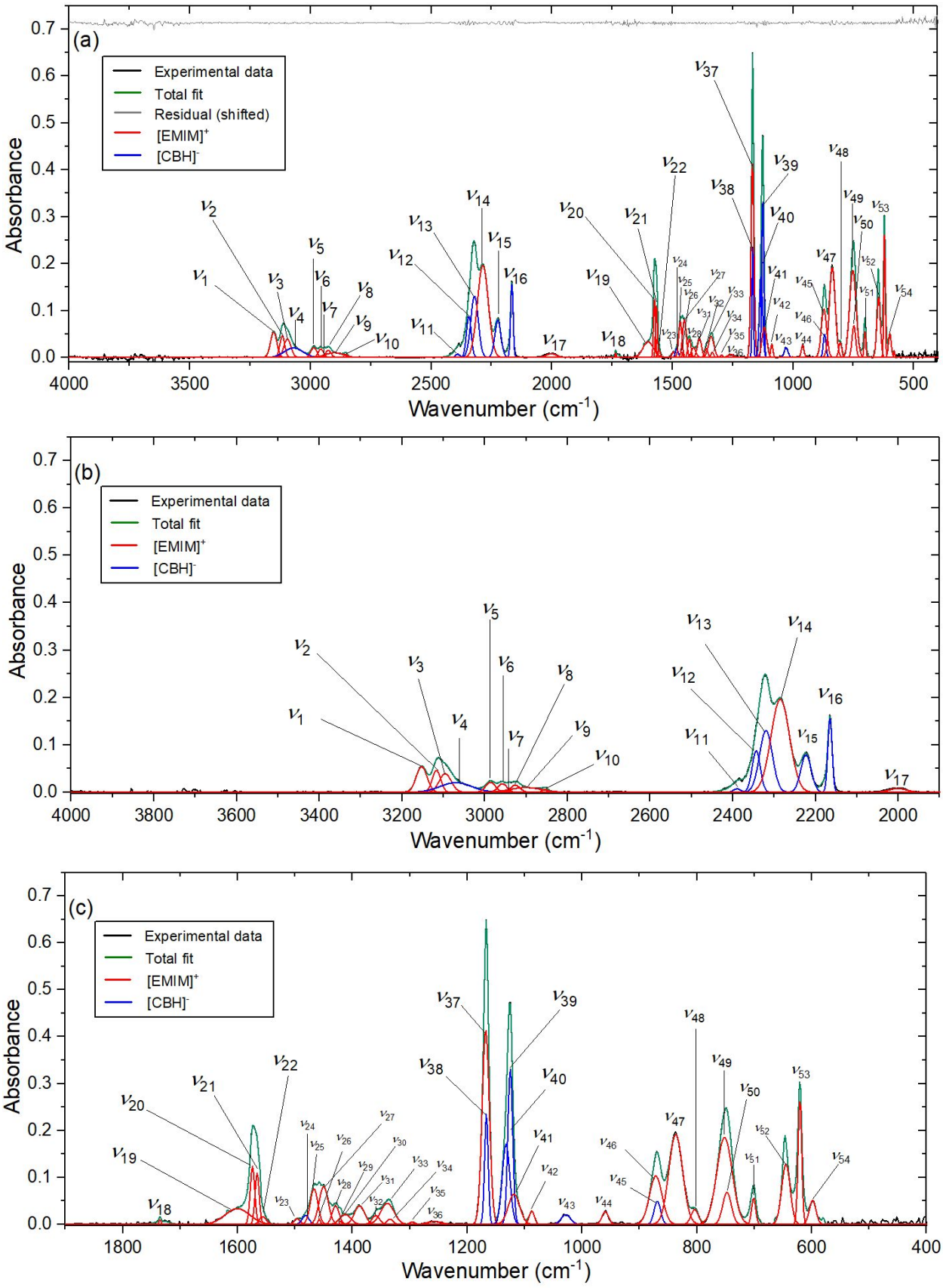
(a)
Experimental data
Total fit
Residual (shifted)
[EMIM]+
[CBH]-
Absorbance
Wavenumber (cm-1)
(b)
Experimental data
Total fit
[EMIM]+
[CBH]-
Absorbance
Wavenumber (cm-1)
(c)
Experimental data
Total fit
[EMIM]+
[CBH]-
Absorbance
Wavenumber (cm-1)

Figure 4. FTIR spectrum with deconvolution for the ionic liquid [EMIM][CBH]; - (a) full range (4000-400 cm^{-1}), (b) 4000-1900 cm^{-1} and (c) 1900-400 cm^{-1}.

Table 2: Assignment of the bands/peaks in the FTIR spectrum of the hypergolic ionic liquid [EMIM][CBH].[55-57]

Band	Vibrational mode description	Measured wavenumber (cm^{-1}) (this work)	Literature wavenumber (cm^{-1}), intensity
ν_1	ν (aro C-H)	3152	3166, s
ν_2	ν (aro C-H)	3116	3125, s
ν_3	2 × ν (C═C)	3095	(2 × 1576), sh, w
ν_4	ν^{a1} (C-N) + ρ^{e} (B-H)	3066	(2179 + 890), m
ν_5	ν_{as} CH_3 (Me)	2986	2989, m
ν_6	ν_{as} CH_3, CH_2	2961	2970, sh, w
ν_7	ν_{as} CH_3 (Et)	2941	2952, w
ν_8	ν_s CH_2	2923	2917, vw
ν_9	ν_s CH_3 (Et)	2892	2892, vw
ν_{10}	δ_{as} CH_3 (Me)	2854	(2 × 1458), vw
ν_{11}	ν_e (B-H)	2390	2390, m
ν_{12}	ν_e (B-H)	2345	2350, sh
ν_{13}	ν_e (B-H)	2320	2320, s
ν_{14}	2 × *ν* (C_{ali}-N), *r*(ali)	2286	(2 × 1172), s
ν_{15}	ν^{a1} (B-H)	2224	2240, m
ν_{16}	ν^{a1} (C≡N)	2166	2179, s
ν_{17}	*ν* (C_{ali}-N), *r*(ali) + r (CH_2), r (CH_3) (Et)	2000	(1172 + 805), vw
ν_{18}	*ν* (C_{ali}-N), *r*(ali) + ν N-Et, ν N-Me	1736	(1172 + 598), vw
ν_{19}	-	1602	1619, sh
ν_{20}	ν (C═C)	1575	1576, s
ν_{21}	ν_{as} (N-C-N), R (C-H)	1566	1571, sh
ν_{22}	-	1557	-
ν_{23}	*ν* (C_{ali}-N), *r*(ali) + δ (N-Et)	1497	(1172 + 381), vw
ν_{24}	δ^{a1} (B-H) + δ^{e} (BCN)	1482	(1135 + 358), vw
ν_{25}	δ_{as} CH_3 (Et)	1466	1462, m
ν_{26}	δ_{as} CH_3 (Me)	1458	1458, m
ν_{27}	r CH_2, r CH_3(Et) + γ N-Et, γ N-Me	1451	(805 + 649), m
ν_{28}	δ_s CH_3	1430	1432, w
ν_{29}	r CH_2, r CH_3(Et) + γ N-Me, ring puckering	1420	(805 + 623), w
ν_{30}	2 × (γ N-Me, ring puckering)	1412	(2 × 623), w
ν_{31}	δ_s CH_3 (Et), w CH_2	1390	1392, w
ν_{32}	w CH_2	1357	1358, vw

ν_{33}	ν N-Et, N-Me, breathing	1339	1337, w
ν_{34}	ν N-Et, N-Me + γ N-Et, γ N-Me	1334	(702 + 649), w
ν_{35}	t CH_2	1296	1300, sh, w
ν_{36}	r C-H	1257	1250, vvw
ν_{37}	r C-H, ν N-Et, N-Me,	1168	1172, s
ν_{38}	δ^e (B-H)	1166	1195, m
ν_{39}	δ^{a1} (B-H)	1133	1145, sh, w
ν_{40}	δ^{a1} (B-H)	1126	1135, s
ν_{41}	r CH_3	1119	1120, sh
ν_{42}	-	1088	vvw
ν_{43}	δ^{a1} (B-H)	1026	1020,w
ν_{44}	ν (C-C) (Et)	959	960, w
ν_{45}	γ C-H	872	896, w
ν_{46}	r^e (B-H)	869	890, w
ν_{47}	γ C-H	837	849, m
ν_{48}	r CH_2, r CH_3(Et)	804	805, w
ν_{49}	-	756	-
ν_{50}	δ (N-Et)	748	(2 × 381), vvw
ν_{51}	ν N-Et, ν N-Me	701	702, w
ν_{52}	γ N-Et, γ N-Me	644	649, m
ν_{53}	γ N-Me, ring puckering	621	623, m
ν_{54}	ν N-Et, N-Me	598	598, w

Abbreviations used: vw, very weak; vvw, very very weak; w, weak; m, medium; s, strong; vs, very strong; sh, shoulder; ν_s, symmetric stretch; ν_{as}, asymmetric stretch; ν (X-Y), stretch between X and Y atoms; ν_i, indexed bands from the FTIR spectrum in Figure 4; *δ*, bend; t, torsion; *w*, wagging; *r*, rocking; *γ*, out of plane; aro, aromatic; ali, aliphatic; *e*, approximated band assignments in the literature [Ref. 55-57]

It is evident that compared to the Raman spectrum, the number of infrared allowed transitions are found to be higher in the FTIR spectrum; the latter contains a significant number of infrared allowed combination bands contributing to the overall spectrum. In the high wavenumber region, the bands labelled as ν_1 and ν_2 at 3152 and 3116 cm^{-1} are assigned to the stretching vibrations of the aromatic C-H bonds. The bands from ν_5 to ν_{10} in the range of 3000-2800 cm^{-1} correspond to the symmetric and asymmetric stretching vibrations of the aliphatic methyl and ethyl chains in the $[EMIM]^+$ moiety. In the 2400 to 2200 cm^{-1} region, several bands (ν_{11}, ν_{12}, ν_{13}, ν_{15}) were identified as characteristic B-H stretches for the CBH anion, whereas the -C≡N stretching vibration is marked as the ν_{16} band (2166 cm^{-1}). The C=C stretching vibration and the NCN bending for the

imidazolium ring are located at 1575 cm^{-1} (ν_{20}) and 1566 cm^{-1} (ν_{21}); the overtone of the former appears as a weak peak at 3095 cm^{-1} (ν_3). It is noticeable that the blue section of the fingerprint region, i.e. the 1500-1200 cm^{-1} segment of the spectrum, is highly congested and most of the features (ν_{23}, ν_{25} to ν_{36}) belong to the bending vibration corresponding to N-methyl, N-ethyl linkages (C-N-C) and methyl, ethyl groups (-CH_2) of the cationic part. Unlike in the Raman spectrum, the bending modes for the -BH_2 functional group appear at higher intensities at 1166, 1133, 1126 cm^{-1}; these are labelled as ν_{38}, ν_{39} and ν_{40}, respectively. There is a cluster of features below 1000 cm^{-1} in the low wavenumber segment; predominantly, these features can be assigned as the rocking, ring puckering and out-of-plane bending vibrations from the functional groups of the cation $[EMIM]^+$.

3.1.3. Raman spectra of the oxidizer (HNO_3)

The Raman spectra of the levitating droplet of 70 % and 30 % aqueous nitric acid (HNO_3) solutions in argon are presented in Figure 5, while the same for 10 % and 20 % are supplied in Figure S7. The spectral traces were deconvoluted, and the resulting peaks are listed in Table 3. It is well-established that aqueous nitric acid undergoes acid dissociation via equation (2).[58]

$$HNO_3 + H_2O \leftrightarrow H_3O^+ (aq) + NO_3^- (aq) \quad (2)$$

In all Raman spectra, bands of these three species (HNO_3, NO_3^-, H_2O) were identified; these were distinguished using differently colored traces after the spectral deconvolution according to the literature values.[58-60] In the high wavenumber region (3800-2500 cm^{-1}) the broad band is assigned of hydrogen-bonded symmetric and asymmetric O-H stretches of water (ν_2, ν_3 and ν_4) as well as weak features from O-H stretch of HNO_3 (ν_1).

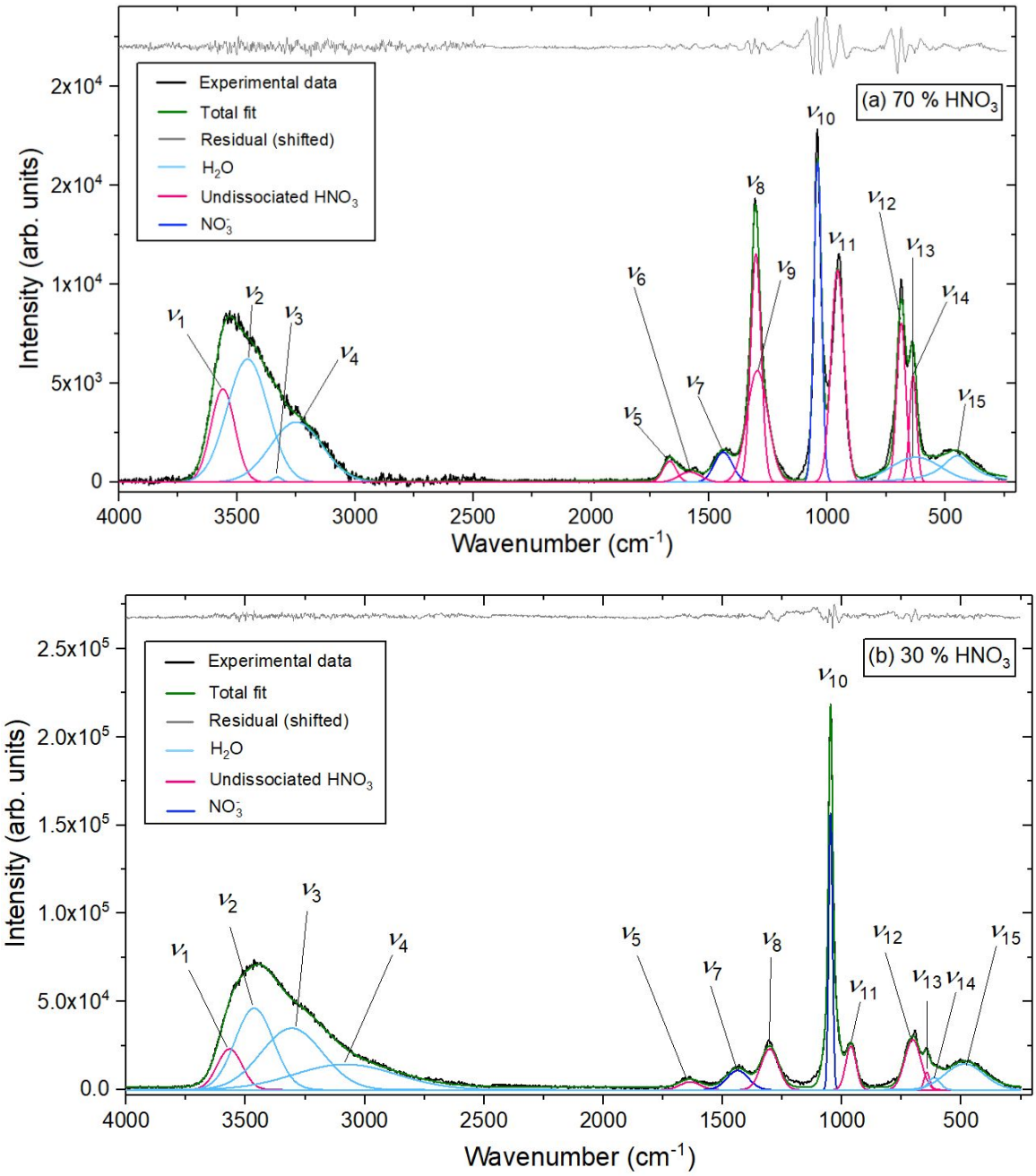

Figure 5. Raman spectra with deconvolution for the aqueous solutions of nitric acid (HNO_3) in the range 4000-200 cm^{-1} for concentrations- (a) 70 % and (b) 30 %.

Table 3: Assignment of the bands/peaks in the Raman spectrum for nitric acid (HNO_3) solutions.

Band	Vibrational mode description	Measured wavenumber (cm^{-1}) (this work)	Literature wavenumber (cm^{-1}), intensity
ν_1	O-H stretching of HNO_3	3560	3551, s

ν_2	O-H stretching of H_2O	3456	3511, s
ν_3		3329	3393, s
ν_4		3246	3233, s
ν_5	NO_2 asymmetric stretching	1668	1679, w
ν_6	HO-NO_2 stretching + NO_2 bending	1563	1607, w
ν_7	NO_3^- asymmetric stretching	1436	1430, w
ν_8	NO_2 symmetric stretching	1305	1341, s
ν_9	2ν NO_2 bending	1296	1298, w
ν_{10}	NO_3^- symmetric stretching	1046	1057, w
ν_{11}	HO-NO_2 stretching	952	930, s
ν_{12}	NO_2 bending	684	677, m
ν_{13}	Librational mode of H_2O	642	650, w
ν_{14}	HO-NO_2 bending	629	611, m
ν_{15}	Librational mode of H_2O	442	430, w

Abbreviations used: w, weak; m, medium; s, strong, ν_i, indexed bands from the Raman spectrum in Figure 5. [Ref. 58-60]

The spectral traces are enriched with peaks from the undissociated HNO_3, such as the NO_2 symmetric (ν_8) and asymmetric (ν_5) stretches appearing at 1305 and 1668 cm^{-1}, respectively. Whereas, the 684 (ν_{12}) and 952 cm^{-1} (ν_{11}) absorptions are assigned to the NO_2 bending mode and the HO-NO_2 stretching mode, respectively. The first overtone of ν_{12} can be located at 1296 cm^{-1} (ν_9) and the combination of ν_{11} and ν_{12} appears as ν_6 (1563 cm^{-1}) band. It is notable here that the features of undissociated HNO_3 are much prominent in the spectral trace (a) for 70 % HNO_3 and the corresponding intensities got diminished upon dilution (trace (b)). Dilution in aqueous medium also results in generation of nitrate ion (NO_3^-) through reaction (2) and vibrational features at 1436 (ν_7) and 1046 cm^{-1} (ν_{10}) indicate the asymmetric and symmetric stretches, respectively.[58] Although the NO_3^- symmetric stretching has been tagged as a weak feature in the literature for pure HNO_3, in our spectra due to preferred acid dissociation (2) in the aqueous medium, the concerned peak (1046 cm^{-1}) becomes much stronger. Further, in the extreme low wavenumber section of the spectra, the bending mode for HO-NO_2 (ν_{14}) and librational modes (ν_{13}, ν_{15}) for water dominate.

3.2. High-speed imaging of the droplet merging and reactions

3.2.1. Optical camera images

The high-speed optical camera captures fast events at a repetition rate up to 1 kHz. Merging videos

were recorded individually for droplets of 10, 20, 30 and 70 % HNO_3 with the ionic liquid [EMIM][CBH]; these are supplied in the Supplementary Information as Movie S1, Movie S2, Movie S3 and Movie S4, respectively. Figure 6 depicts the series of temporally resolved optical images extracted from the videos for merging of (A) 10 %, (B) 20 % and (C) 30 % HNO_3 with a droplet of the ionic liquid [EMIM][CBH]. The first frame (1) for each case represents both the separated levitating reactant droplets referred this to as 'pre-merging'. The lower node contains the ionic liquid droplet, whereas the upper one holds the HNO_3 droplet. In the second frame (2), which is the pivotal 'merging' step, the ionic liquid droplet from the lower node (second node) approaches to the upper node (third node) upon amplitude modulation achieved by using a frequency chirp of 1-50 Hz from a waveform generator. Essentially this frame demonstrates the upward merging motion of the ionic liquid droplet. Once the merged droplet is formed, as shown in the frame (3) it becomes stable at the upper node and as time progresses, the formation of gas bubbles as the result of a chemical reaction, is evident; these are more apparent from the latter frames (4-5-6) for each concentration of HNO_3. It is also evident from these images that the extent of bubble formation increases as the HNO_3 concentration rises; this indicates the occurrence of instantaneous reactions upon merging, which produces gaseous products. For 10 % HNO_3, the merged droplet survived longer at the pressure node of the levitator typically over 10 s. However, in the case of 20 % and 30 % HNO_3, as the formation of bubbles accelerates, the droplets detrapped much earlier. We noted a drastic consequence when the ionic liquid droplet was merged with 70 % HNO_3 droplet (Movie S4); the optical snapshots of this merging event are chronologically shown in Figure 7. Frames 1 and 2 represent the pre-merging stage of the droplets and the merging approach of the ionic liquid, respectively. Frame 3 depicts the merged droplet, but within 4 ms, the droplet becomes glassy as displayed in frame 4. From frame 5 to 8, a series of fast chemical reactions can be noticed resulting an elevated production of gases and ejection of the liquid from the merged droplet. A close look at the images also reveals the generation of greenish white fumes surrounding the droplet.

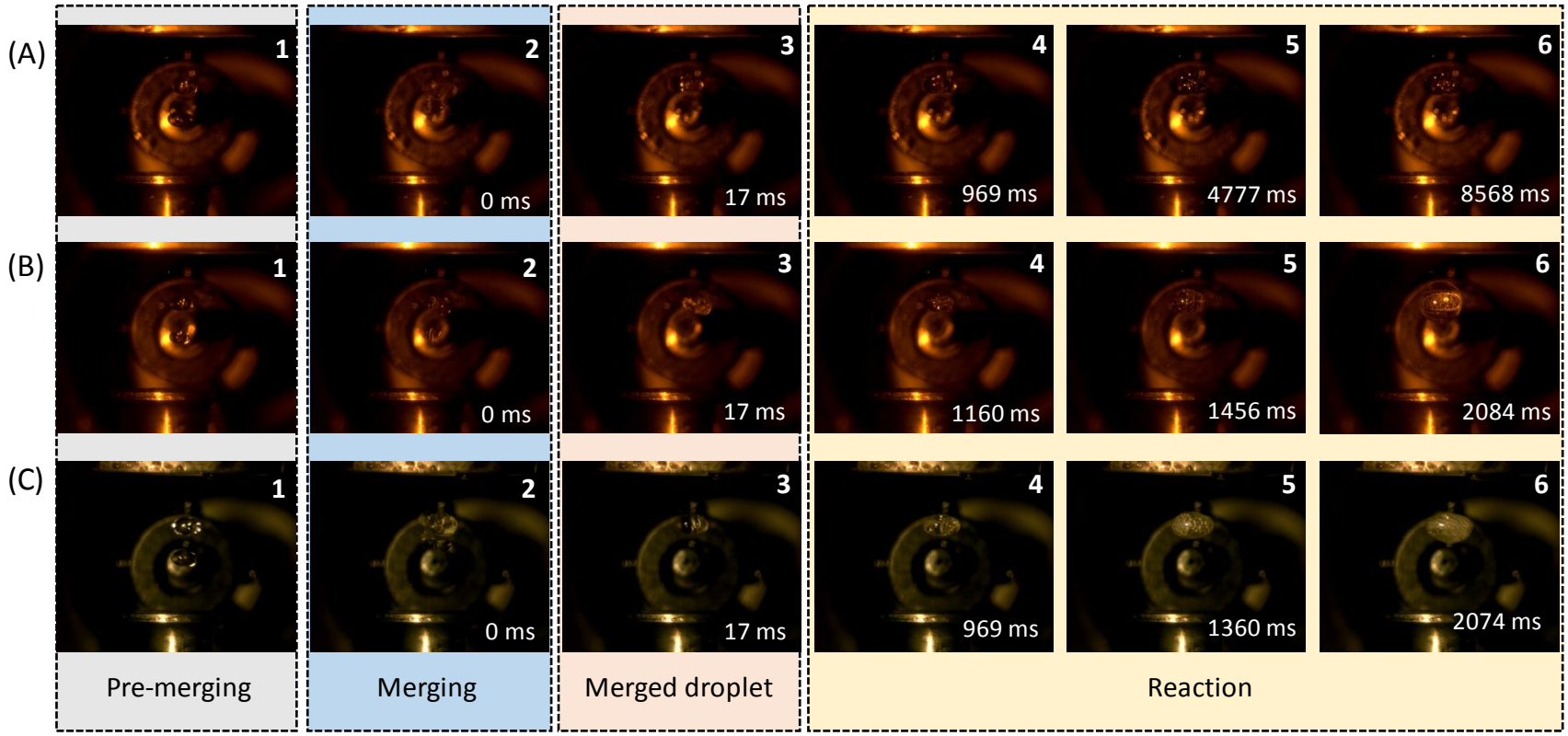

Figure 6. Snapshots captured by the high-speed optical camera showing the merging and successive reactions of ionic liquid [EMIM][CBH] + HNO_3 aqueous solutions of concentrations- (A) 10 %, (B) 20 % and (C) 30 %. In each case gaseous products were evolved and bubbles can be seen forming in the merged droplet.

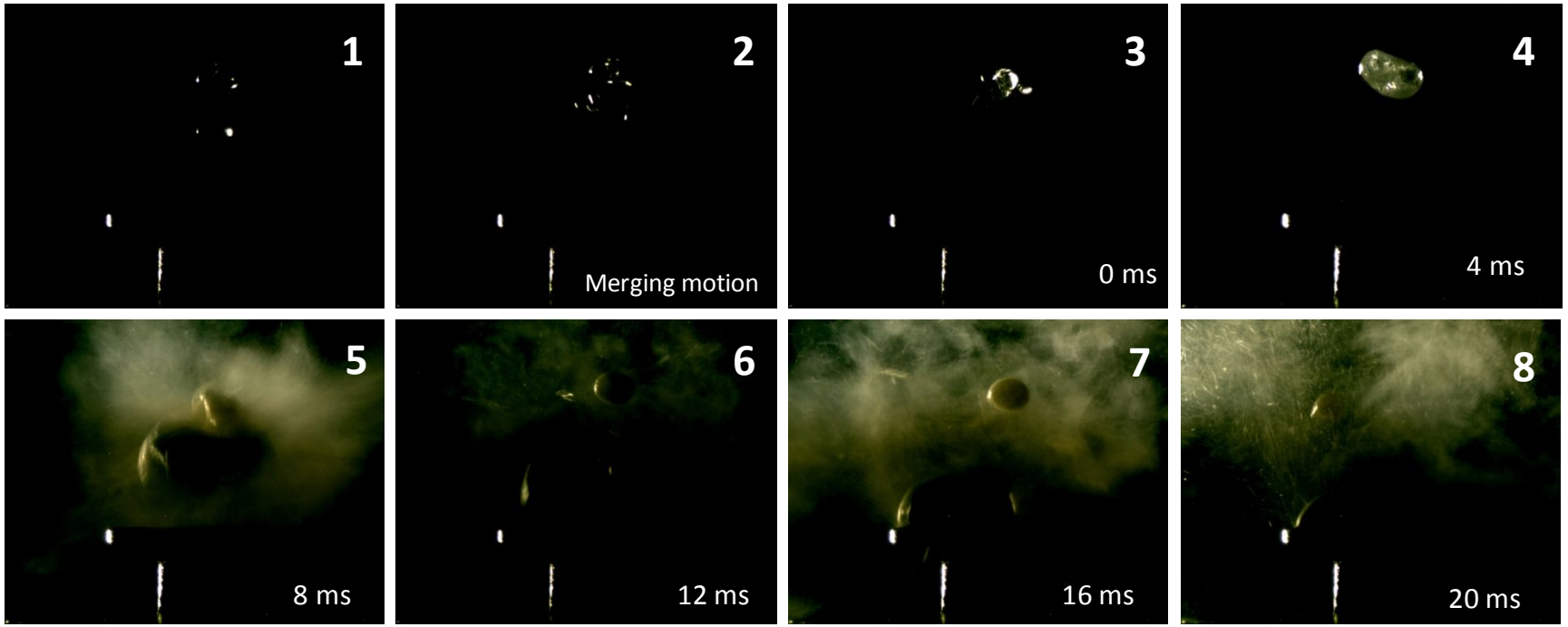

Figure 7. Snapshots captured by the high-speed optical camera depicting the merging and subsequent reactions of ionic liquid [EMIM][CBH] and 70 % HNO_3 aqueous solution showing immense gas release and liquid spillage upon merging.

As a result of this reaction, the merged droplet was found to be detrapped significantly faster compared to the experiments with diluted HNO_3 droplets (10 %, 20 %, 30 %); typically, the droplet survived only a few tens of milliseconds. We also determined the collision energy between the droplets during the merging; here, the HNO_3 droplet in the upper node was assumed to be at rest and the velocity of the approaching ionic liquid droplet was determined from the snapshots of the optical camera. The collision energies determined do not exceed 2 J mol^{-1} (Table S2).

3.2.2. Infrared camera images

The high-speed infrared camera was employed to complement the optical camera images with the time dependent spatial temperature distributions for the droplets at a repetition rate of 250 Hz in steps of 4 ms. Figure 8 depicts the frames captured by the infrared camera during merging followed by the reactions for different HNO_3 concentrations ((A)10 %, (B) 20 %, (C) 30 %). For each of the frames, the temperature scale is shown on the right. Detailed movies have been provided as Supplementary Information- Movie S5, Movie S6 and Movie S7 for 10 %, 20 %, and 30 % of aqueous HNO_3 solutions, respectively. Frame 1 of Figure 8 (for A, B and C) represents the pre-merging stage for both the levitating droplets followed by frame 2, which is indicative of upward merging approach for the ionic liquid droplet. It is interesting to note that for all cases, the initial contact of the droplets of ionic liquid and HNO_3 is linked to an instantaneous temperature rise (frame 2) to temperatures of 323 K, 309 K and 319 K, respectively. In frame 3, although merged, the liquids of the droplets are yet to be mixed homogenously. The reason for such initial inhomogeneity after merging might be linked to the different viscosities of the ionic liquid (0.019 Pa-s at 298 K) and aqueous solutions of the acid (about 0.001 Pa-s at 298 K).[18, 61, 62] The inhomogeneous nature of the merged droplet is also visible in the optical camera videos, although they seem to be more subtle in nature. A significant growth of the merged droplet is also witnessed for frame 5 and 6; the extent of the volume growth by 800 % is quite remarkable in the case of 30 % HNO_3 (C) corroborating a much faster reaction and gas release. As the reaction proceeds (frames 4-6) after merging, a gradual rise in temperature is also noticed from the thermal mapping scale inscribed in the frames shown; the outcome can be simply described as the manifestation of an exoergic reaction between the ionic liquid and HNO_3.

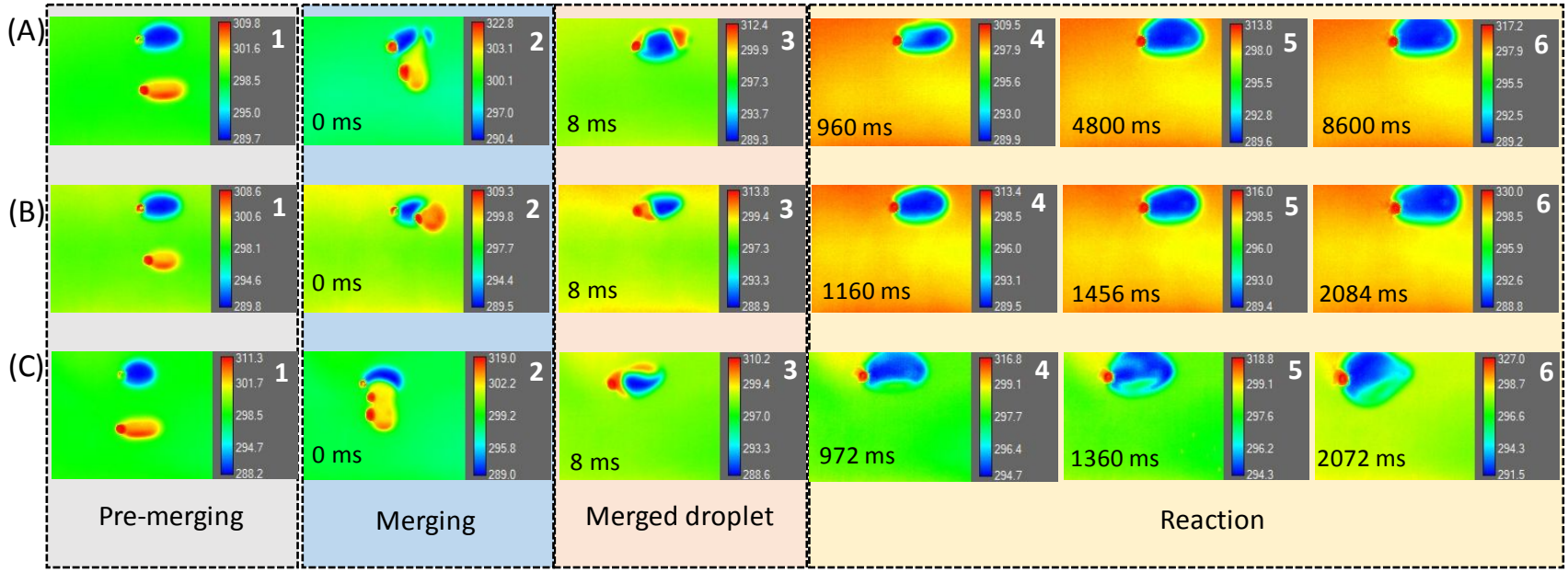

Figure 8. Thermal images captured by the high-speed infrared camera for the reaction of ionic liquid [EMIM][CBH] + HNO_3 aqueous solution of concentrations- (A) 10 %, (B) 20 % and (C) 30 %. Temperature (in Kelvin scale) rise was observed in each case after merging of the droplets.

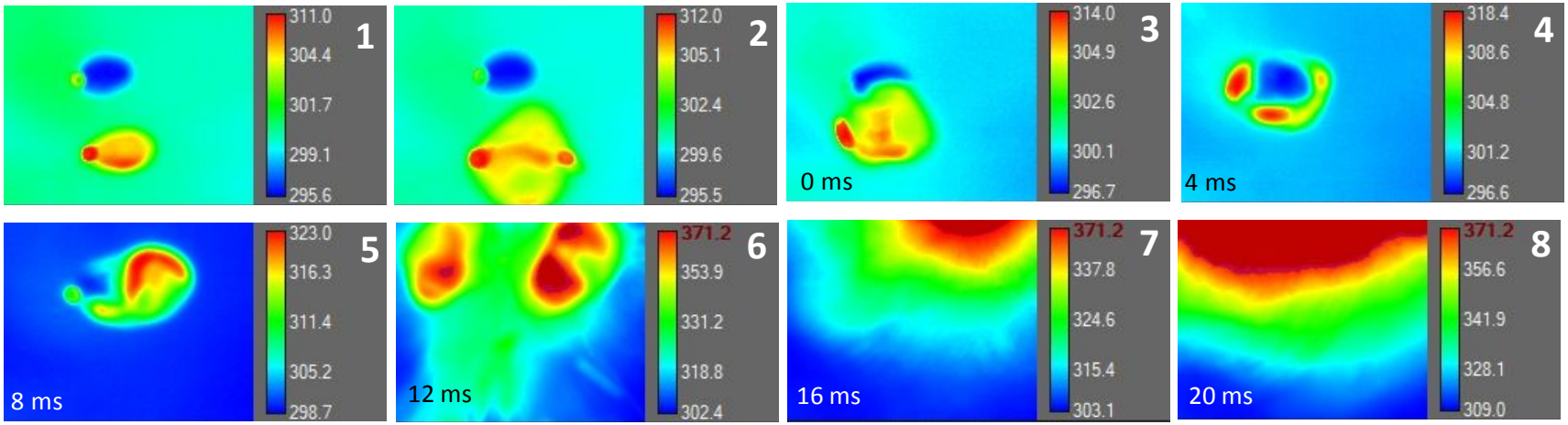

Figure 9. Thermal images captured by the high-speed infrared camera for the reaction of ionic liquid [EMIM][CBH] + 70 % HNO_3 aqueous solution indicating instantaneous temperature (in Kelvin scale) rise upon merging.

Similar to the observations from the optical camera snapshots, the high reactivity between the ionic liquid and 70 % HNO_3 droplets was also perceived by recording an infrared movie (Movie S8) of the merging; the sequentially extracted snapshots are displayed in Figure 9. Frame 1 and 2 represent the pre-merging stages where the latter demonstrates the induced oscillations provided by the frequency chirp in the ionic liquid droplet positioned in the bottom node. Frame 3 distinctively shows the initial merging of the two droplets; a temperature rise is noted for the following frame (4) from 314 to 318 K. It takes only around 8 ms for a homogenous mixing of the reactant droplets; a further temperature increase to 323 K is noted in frame 5. However, the most remarkable step is depicted in frame 6, where a temperature jump from 323 to 371 K was recorded and the droplet bursts into smaller droplets. Eventually, the measured temperature during this reaction exceeded the temperature range of 372 K of the filter used in the infrared camera. To determine the actual temperature, the experiment was also performed with a filter for a higher temperature range and selecting only the merging area as region of interest in the infrared camera software; this resulted in a peak temperature of 435 K. Frame 7 and 8 visualize the significant expansion in volume of the droplet by at least ten times and ejection of the liquid.

3.3. Temperature profiles with time

The temporal plots of the temperature during and after merging were obtained from the high-speed infrared camera with a resolution of 4 ms (Figure 10). For (a) 10 %, (b) 20 % and (c) 30 % of HNO_3 solutions, a temperature spike can be observed initially near 0 ms; this is caused by the merging and mixing of the both reactants. A representative calculation for the enthalpy changes due to mixing of the droplet merging is shown in Table S3; this results in molar enthalpy changes in the range of about 3 to 10 kJ mol^{-1}. The common trend in the post-merging phase is a gradual rise in temperature with time. We noted a steady temperature increase in the case of 10 % HNO_3 with the temperature approaching nearly 320 K before the droplet detrapped. However, for 20 and 30 % of HNO_3, significant fluctuations in the temperature reading were observed. Those fluctuations correspond to the release of gaseous species, which have been formed during chemical reactions, from the droplet. On the other hand, faster removal of the products from the confined merged droplet accelerates the rate of the forward reactions between the remaining reactants resulting an overall rise in temperature at the end to about 330 K.

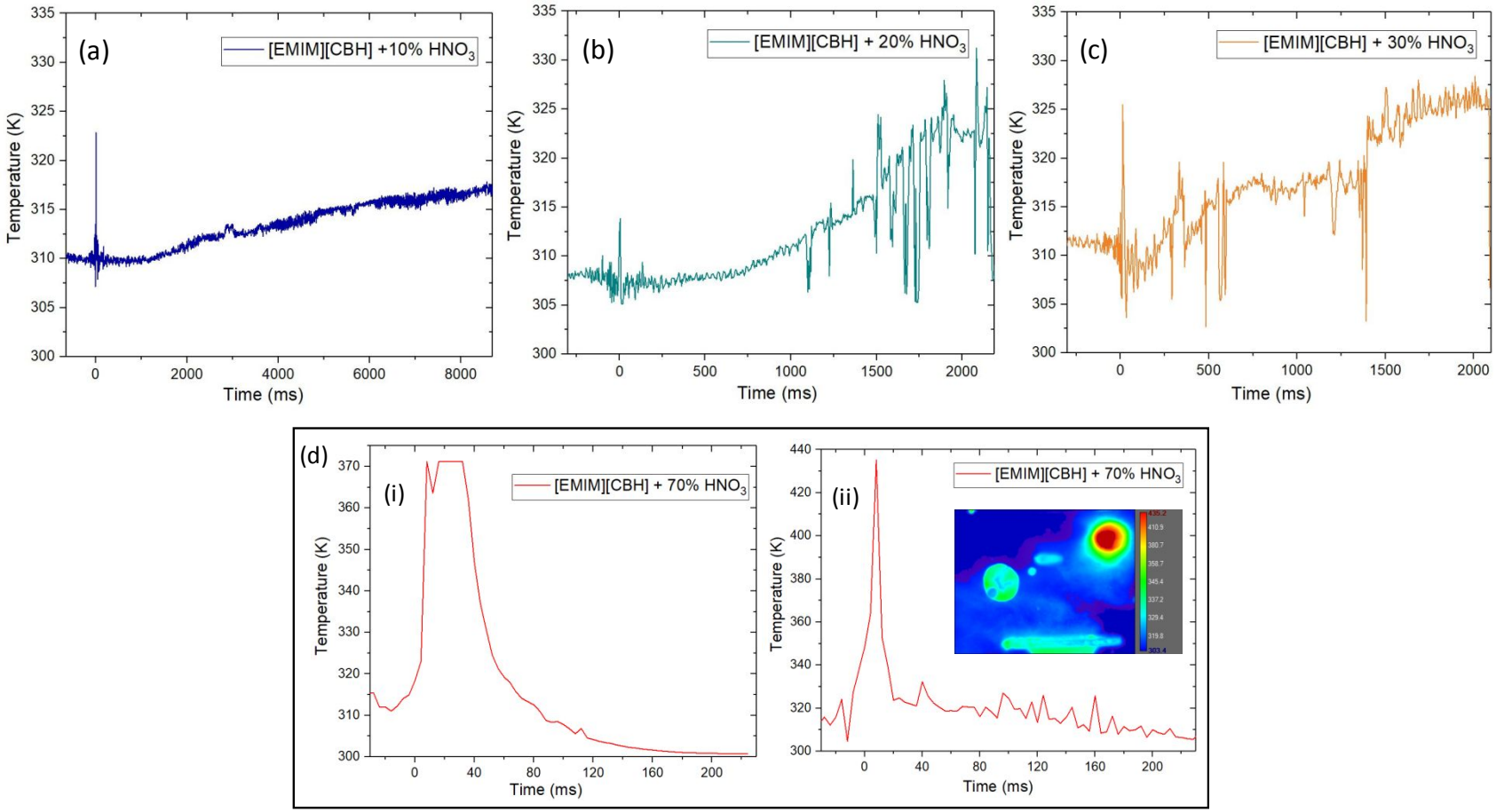

Figure 10. Temperature profiles versus time during merging followed by reactions, measured by the infrared camera, for the reactions of ionic liquid [EMIM][CBH] with aqueous solutions of nitric acid of different concentrations; - (a) 10 %, (b) 20 %, (c) 30 % and (d) 70 %. For 70 % HNO_3, the measured temperature exceeded the temperature range (283-372 K) chosen in the case of (i), showing a saturation effect. In (ii), the maximum temperature (435 K) after merging was recorded using the higher temperature range (353-473 K) and the corresponding thermal image is displayed in the inset.

Extensive and continuous release of gaseous products destabilizes the droplets in the acoustic trap finally causing it to collapse. On contrary, the temperature versus time plot for 70 % HNO_3 (Figure 10(d)) depicts a sharp rise in temperature immediately after merging; within a few milliseconds (12 ms), the system reaches a peak temperature of 435 K as evident from Figure 10(d)(ii). The part (ii) of the figure is added by extracting the temperature reading for the reactive zone of the droplet as discussed above to account for the saturation effect in the recorded temperature profile for part (i).

3.4. FTIR spectroscopy for the detection of gaseous products

3.4.1. Qualitative analysis

The gaseous products formed upon merging between the ionic liquid ([EMIM][CBH]) and the oxidizer (HNO_3) were detected by using FTIR spectroscopy, where the infrared beam passes horizontally across the process chamber (Figure 1). The recorded spectra after merging with four distinct concentrations of HNO_3 ((a) 10 %, (b) 20 %, (c) 30 %, (d) 70 %) are shown in Figure 11; reference spectra were adopted from the HITRAN database for potential products hydrogen cyanide (HCN), nitrous oxide (N_2O), nitric oxide (NO), and nitrogen dioxide (NO_2).[63] Inside the process chamber, HNO_3 is prone to evaporate from the droplets. Hence, the gas phase spectrum of HNO_3 was also added to Figure 11. Starting from the higher wavenumber range, the weak feature at 3590-3500 cm^{-1} can be correlated with the O-H stretching mode (3550 cm^{-1}) of the HNO_3 vapor; as the HNO_3 concentration increases from 10 % to 70 %, this band becomes easily recognizable. The existence of this species can be confirmed through, e.g., the NO_2 asymmetric stretching, the NO_2 symmetric stretch, and the NO_2 in-plane bending revealed in the spectra at 1750-1670, 1355-1265, and 930-840 cm^{-1}, respectively. The broad band spanning 3375-3240 cm^{-1} can be assigned to the C-H stretch (3311 cm^{-1}) of HCN; the corresponding bending mode (712 cm^{-1}) was identified at 770-650 cm^{-1} revealing the characteristic Q-branch. N_2O was also detected in all spectra with the characteristic asymmetric stretching vibration (2224 cm^{-1}) in the 2260-2170 cm^{-1} region. The broad, weak absorptions at 2940-2880 cm^{-1} for the spectrum of the merged 70 % HNO_3 (Figure 11 (d)) indicates the presence of NO_2 (combination bands); however, for the mergers with dilute acids, that feature was not observable. Similarly, the fundamental stretch at 1617 cm^{-1} for NO_2 was very intense in the 1650-1570 cm^{-1} region. Finally, we would like to state that no evidence for gas phase NO was detectable in any merging event. Therefore, we can conclude qualitatively that HCN

and N_2O are generated in all merging processes with the ionic liquid from 10 % to 70 % nitric acid; however, NO_2 was only detectable during the merging process with 70 % nitric acid.

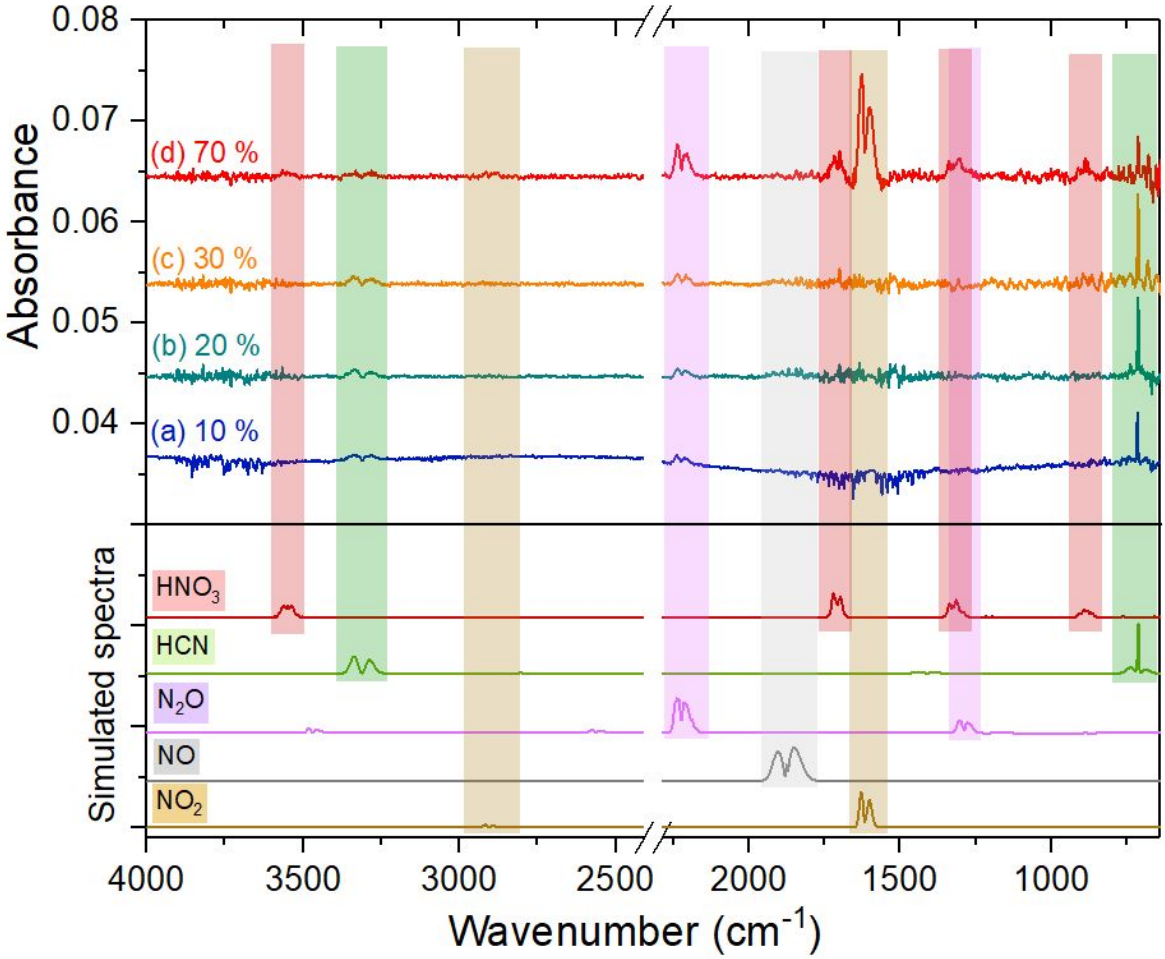

Figure 11. FTIR spectra identifying the gaseous products formed due to merging of ionic liquid [EMIM][CBH] with the aqueous solution of HNO_3 of concentrations; - (a) 10 %, (b) 20 %, (c) 30 % and (d) 70 %. In the lower section of the plot, simulated FTIR spectra of the reference gases (HNO_3, HCN, N_2O, NO and NO_2) are also shown. The break in the x-axis is introduced to mask the background absorbance due to carbon dioxide (CO_2).

Both the ionic liquid and the oxidizer contain nitrogen. In order to identify to what extent HCN, N_2O, and NO_2 were generated from the ionic liquid ([EMIM][CBH]) or the oxidizer, we conducted a droplet merging experiment of the ionic liquid with a non-oxidizing, non-nitrogenous acid.

Hydrochloric acid (HCl) was chosen at a concentration of 12 %. The FTIR spectra for the gaseous products evolved from the merging are depicted in Figure 12.

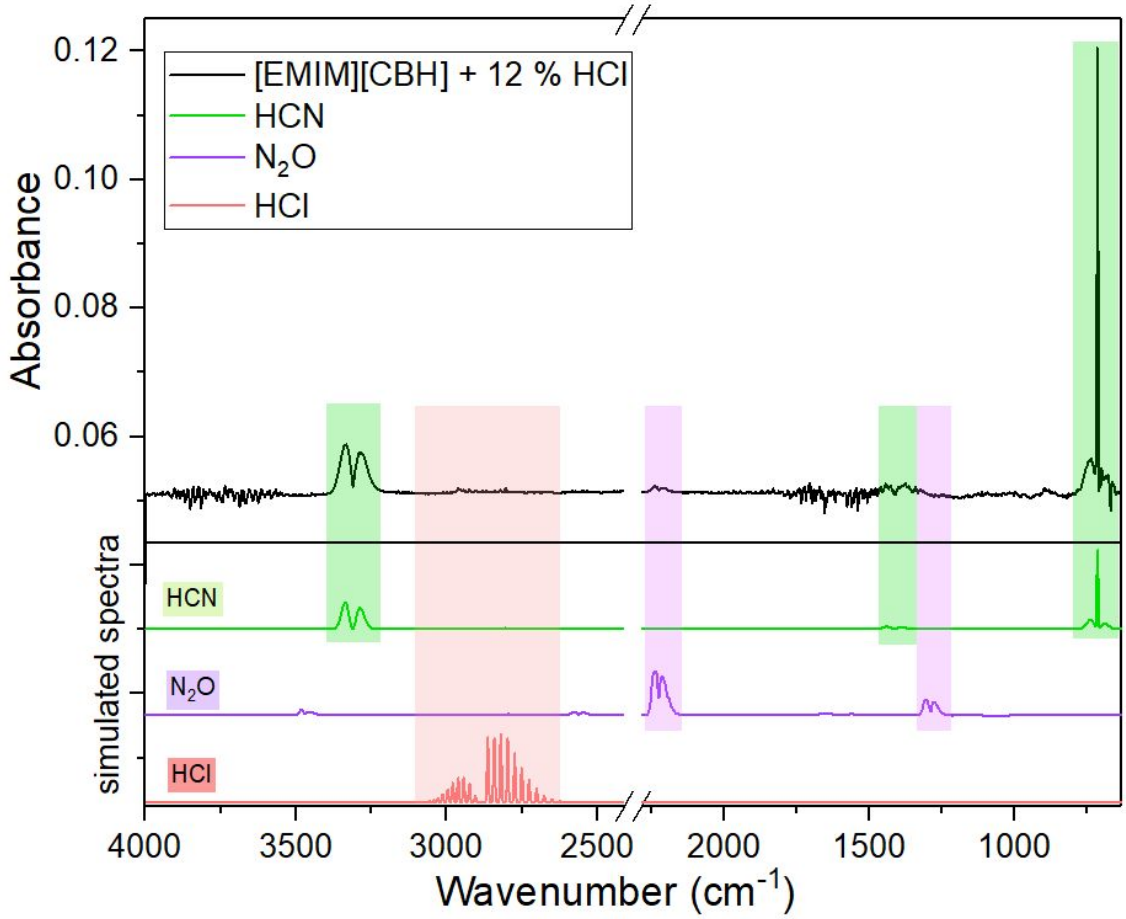

Figure 12. FTIR spectrum (black trace, topmost) detecting the gases produced upon merging of ionic liquid [EMIM][CBH] with the aqueous solution of 12 % HCl (w/w). In the lower section of the plot, simulated FTIR spectra of the reference gases (HCN, N_2O and HCl) are also shown. The break in the x-axis is introduced to mask the background absorbance due to CO_2.

First, neither NO_2 nor NO was detectable. This finding provides evidence that the NO_2 detected from the merging of the ionic liquid with 70 % nitric acid originated from the acid, but *not* from the ionic liquid. *Second*, the production of HCN due to merging is evident from the intense bands at 3375-3240 cm^{-1} and 770-650 cm^{-1} regions. Therefore, we may conclude that HCN originates from the ionic liquid, more specifically the source of the nitrogen atom is the HIL. *Finally*, a small

absorption covering the range of 2260-2170 cm^{-1} indicates the presence of N_2O (asymmetric stretch). This finding is quite intriguing since neither the hydrochloric acid nor the ionic liquid contains any oxygen. This suggests that the aqueous medium (H_2O) represents the source of the oxygen atom in N_2O at least in the merger for ionic liquid – hydrogen chloride acid solution; hence revealing an active chemistry of the solvent.

3.4.2. Quantitative analysis

The gaseous reaction products were further quantified from their calibration curves obtained by using respective gases individually in the process chamber (Supplementary Information Figures S3-S6). Table 4 displays the number of moles of the reactants and the gas phase products along with the branching ratios for the latter. In case of 10-30 % HNO_3, the major products found are HCN and N_2O; their branching ratios are calculated up to 58 % and 54 %, respectively, with only smaller contributions from NO_2. For the ionic liquid – hydrogen chloride system, HCN represents the major product (98 %) with only minor fractions of N_2O (2 %). Therefore, we can conclude that in the reaction of the protons from both HNO_3 and HCl with the ionic liquid, the ionic liquid represents the source of the cyanide group (-C≡N) in the HCN. As far as the formation pathway of HCN is concerned, a comparison of the functional moieties of the cation and anion of the ionic liquid, the $[CBH]^-$ anion already contains the -C≡N functional group. Therefore, protonation in the CBH moiety followed by the isomerization and subsequent cleavage of the B-C bond may form hydrogen cyanide (HCN). However, for N_2O, two production routes could be identified: a dominating pathway with oxygen originating from the oxidizer (HNO_3) and a minor route – as evident from the experiment with hydrochloric acid (HCl) – with oxygen stemming from the aqueous solvent. Recall that the qualitative considerations (section 3.4.1.) already revealed that NO_2 originated from the oxidizer. The low percentage yields (Table S4) of individual product gases indicate the incomplete reaction caused due to the short survival times before detrapment of the merged droplet. Finally, from the extracted temporal concentration profiles (Figure S8) of the generated gases, a significant growth of HCN and N_2O was found to be common for all of concentrations of HNO_3 used; however, the increase in NO_2 concentration was minimal as the reaction progressed once again implying that NO_2 was generated from the HNO_3. For the IL and HCl merging reaction, the number of moles for HCN has been found to be much higher (2.7×10^{-6} mole) as compared to N_2O (5.0×10^{-8} moles).

Table 4: Number of moles for the reactants- [EMIM][CBH] and the acid (HNO_3 or HCl) solutions; and the gases produced after merging. The branching ratios for the products have also been mentioned in the parentheses. For NO_2, upper limits were computed for merging with 10, 20, and 30 % HNO_3 since the 1650-1570 cm^{-1} absorption might overlap with contributions from the O-H bending from HNO_3.

Strength of acid (w/w)	Reactants				Gaseous products		
	Volume of [EMIM][CBH] droplet (microliter)	[EMIM][CBH] (mol) ($\times 10^{-5}$)	Volume of acid droplet (microliter)	Acid (mol) ($\times 10^{-5}$)	HCN (mol) ($\times 10^{-6}$)	N_2O (mol) ($\times 10^{-6}$)	NO_2 (mol) ($\times 10^{-6}$)
10% HNO_3	12.7 ± 6.0	8.2 ± 3.9	13.0 ± 7.0	2.1 ± 1.1	1.9 ± 0.3 (58 % ± 10 %)	1.2 ± 0.1 (36 % ± 4 %)	0.2 ± 0.1 (6 % ± 3 %)
20% HNO_3	6.6 ± 3.0	4.3 ± 1.9	7.1 ± 4.0	2.4 ± 1.4	0.3 ± 0.1 (41 % ± 11 %)	0.4 ± 0.1 (54 % ± 8 %)	0.03 ± 0.01 (5 % ± 2 %)
30% HNO_3	28.2 ± 1.4	18.3 ± 0.9	15.1 ± 8.0	7.9 ± 4.2	0.4 ± 0.1 (62 % ± 6 %)	0.2 ± 0.1 (32 % ± 12 %)	0.04 ± 0.01 (6 % ± 2 %)
70% HNO_3	7.8 ± 4.0	5.1 ± 2.6	12.8 ± 6.0	19.8 ± 9.3	1.2 ± 0.4 (32 % ± 8 %)	1.5 ± 0.2 (41 % ± 5 %)	1.0 ± 0.03 (27 % ± 11 %)
12% HCl	5.5 ± 1.5	3.6 ± 1.0	15.7 ± 3.8	6.3 ± 1.5	2.7 ± 0.3 (98 % ± 6 %)	0.05 ± 0.01 (2 % ± 1 %)	-

3.5. Raman spectroscopy of the merged droplet

3.5.1. Qualitative analysis

To decipher the chemical reactions that occur during and after the merging process, the merged droplet was probed exploiting pulsed Raman spectroscopy for HIL - HNO_3 systems with HNO_3 concentrations of 30 % (Figure 13) and 10 %, 20 % (Figure S9). As discussed earlier, the reaction of the HIL with 70 % HNO_3 caused an instantaneous detrapping of the merged droplet due to vigorous chemical reactions accompanied by gas formation (HCN, N_2O, NO_2); therefore, no Raman spectra could be recorded at this concentration. To identify newly formed products, the Raman spectra of the acids (a) and the ionic liquid (b) were compared with merged droplets, e.g. (c) and (d). Further, the Raman spectra of the merged droplets were deconvoluted (30%, Figure 13; 20%, Figure S10; 10% Figure S11) with features of the cation $[EMIM]^+$ and anion $[CBH]^-$ of the HIL and of the acid, subsequently they are color coded. Broad features emerged in the merged droplets; within the range of 3800 – 3300 cm^{-1}, these correspond to O-H stretching modes of water (solvent). The sharper bands in the 3200-2800 cm^{-1} region are indicative of $[EMIM]^+$ which remain essentially unaltered in intensity. On the contrary, noteworthy decrease in the peak intensities with respect to the $[CBH]^-$ anion (2400-2100 cm^{-1}) can be observed. These findings suggest at least qualitatively that the acid reacts predominantly with the $[CBH]^-$ anion of the ionic liquid. In detail, in the deconvoluted spectrum (Figure 13), the wavenumbers of the peaks are matched with the corresponding Raman features of the reactants, i.e. the ionic liquid and the acid, compiled in Tables 1 and 3; these are labelled as ν^{IL} and ν^{A}, respectively. The remaining features, which cannot be assigned to the HIL or to the acid can be classified as new features corresponding to the intermediates or products of the reaction between the HIL and the acid. They are distinguished from the reactants through a red color coding of the features and labelled as ν^{P}. The majority of the new features evolved in the region 2500-2100 cm^{-1} with the exception of two peaks at 553 and 1001 cm^{-1}. Overall, the Raman spectra depict evidence of six new bands for the merger with 30 % HNO_3 (Figure 13). Note that in case of complex systems, newly emerging peaks cannot be assigned to individual molecules, but only to functional groups. These assignments are compiled in Table 5.[64]

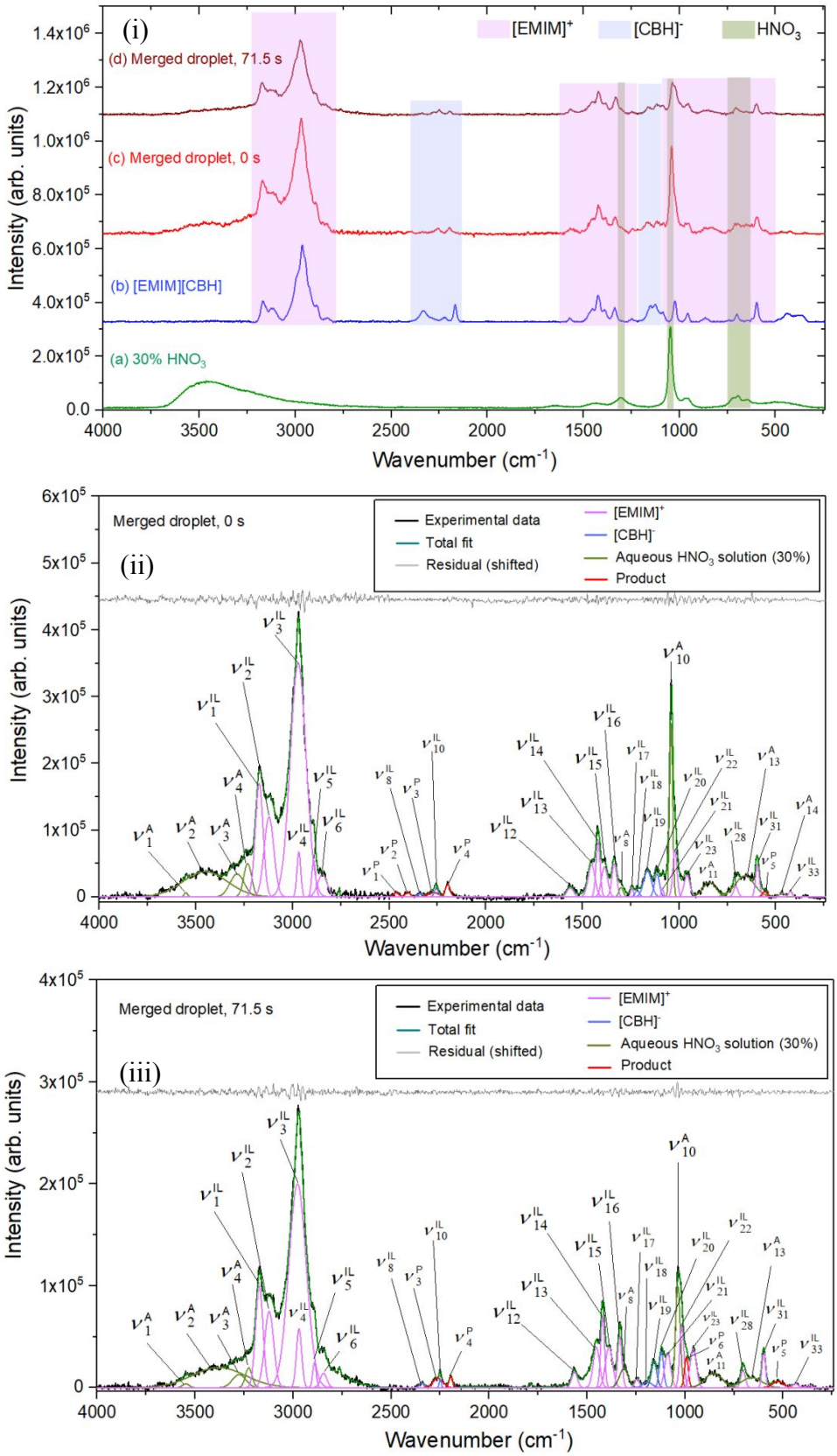

Figure 13. (i) Raman spectra (c and d) of the merged droplet constituting the ionic liquid

[EMIM][CBH] and 30 % HNO_3 undergoing chemical reaction, - (c) at merging and (d) after the reaction. The Raman spectra for the reactants, (a) HNO_3 and (b) [EMIM][CBH] are also presented in the traces below. The characteristic regions of vibrational bands for the cationic ($EMIM^+$) and anionic (CBH^-) components of the ionic liquid, and the acid are highlighted using different color code. Deconvoluted spectra for the merged droplet - at (ii) 0s and (iii) 71.5 s from the merging. The features corresponding to the reactants and the newly formed products/intermediates are distinguished using different color codes and they are labelled with the superscripts, IL (ionic liquid), A (acid) and P (product) for each band (ν).

Table 5: Assignment of the new bands/peaks in the Raman spectra during the reaction between the ionic liquid [EMIM][CBH] and HNO_3 solutions. New peaks in italics were only detected upon reaction with 30 % HNO_3.

Band	Measured wavenumber (cm^{-1}) (this work)	Vibrational mode description	Literature wavenumber (cm^{-1})
ν_1^P	*2465*	B-H stretching/ *asymmetric* BH_2 stretching	2480 2485
ν_2^P	2405	B-H stretching: -BH_3 in mono-substituted borohydride (BH_3X)/ BH_3 in complexes	2400-2200
ν_3^P	2262	ν (NO^+)/ B-H stretching: -BH_3 in mono-substituted borohydride (BH_3X)/ BH_3 in complexes	2267 2400-2200
ν_4^P	2191	Bridged BH_2 stretching	2140-1900
ν_5^P	553	-NC=O deformation	600-550
ν_6^P	*1001*	B-O-H bending/ BH_2 deformation	1012 1150-1000

The band at 2465 cm^{-1} (ν_1^P) can be attributed to B-H stretching and/or asymmetric BH_2 stretching modes; whereas the feature at 2405 cm^{-1} (ν_2^P) corresponds to the B-H stretching of a -BH_3 moiety in a borohydride salt (BH_3-X type) or of complexed BH_3. There could be three possibilities considering the assignment of the 2262 cm^{-1} band (ν_3^P): the stretching mode of the nitrosyl cation (NO^+) or the B-H stretching of BH_3 group in a mono-substituted borohydride or B-

H stretching of bound BH_3. Typical stretching modes of bridged BH_2 moieties can be located at 2191 cm^{-1} (ν_4^P). In the low wavenumber region, the weak feature at 553 cm^{-1} (ν_4^P) can be linked to the -NC=O deformation mode. The peak at 1001 cm^{-1} could be assigned as the B-O-H bending and/or BH_2 deformation mode. The emergence of new peaks in the characteristic $[CBH]^-$ region (2500-2100 cm^{-1}) could be the manifestation of the reaction of the anion with the oxidizer, resulting in key functional groups of boron hydrides (-BH, $-BH_2$, $-BH_3$).

3.5.2. Temporal profiles of reactants

The deconvoluted Raman spectra can be exploited to extract temporal profiles for characteristic Raman-active modes of the reactants and of newly evolving features for the products. Figure 14 represents the time traces of specific bands for the merger of [EMIM][CBH] with 30 % HNO_3 (20 %, Figure S12; 10 %, Figure S13) and it is organized as follows: section (i) highlights temporal changes for the reactants, i.e. HNO_3 (A), $[CBH]^-$ (B), and $[EMIM]^+$ (C); section (ii) compiles the temporal evolution of prominent product peaks. *First*, as a general trend, the features of the acid (912 and 1046 cm^{-1}) decrease as the reaction progresses for all concentrations. *Second*, a similar decay pattern was noticeable for the bands corresponding to $[CBH]^-$ anion at 2334 and 2239 cm^{-1}. *Third*, the vibrational modes of $[EMIM]^+$ such as 1423 and 2964 cm^{-1} decay at a much slower rate as evident from the magnified insets. Quantitatively spoken, the decay of the reactants could be fit with a first-order exponential decay ($A = [A_0]\, e^{-kt}$) with the rate constants compiled in Table 6. Here, the rate constants associated with the decay of HNO_3 and $[CBH]^-$ are within error limits, 0.07± 0.01 s^{-1} versus 0.1 ± 0.01 s^{-1} for 30 % HNO_3 and also identical for 10 % and 20 % HNO_3 (0.010 ± 0.005 s^{-1} versus 0.010 ± 0.005 s^{-1}; 0.04 ± 0.01 s^{-1} versus 0.05 ± 0.01s^{-1}). The associated decay rates increase as the acid concentration rises, but the same for $[EMIM]^+$ are notably smaller by a factor of about 3 (10 %), 5 (20 %), and 14 (30 %). These findings indicate toward the dominating reaction between HNO_3 and $[CBH]^-$, while the cation of the HIL, $[EMIM]^+$, reacts much slower hence implying that reactions of the cation contribute less to the overall reaction mechanism. The slow decay of the $[EMIM]^+$ cation could also be explained in terms of the occurrence of physical processes that result in mass loss of the merged droplet, e.g. bubble formation followed by rupture and spraying of the merged droplet material.

(i) Reactants

(A) 30% HNO_3 bands

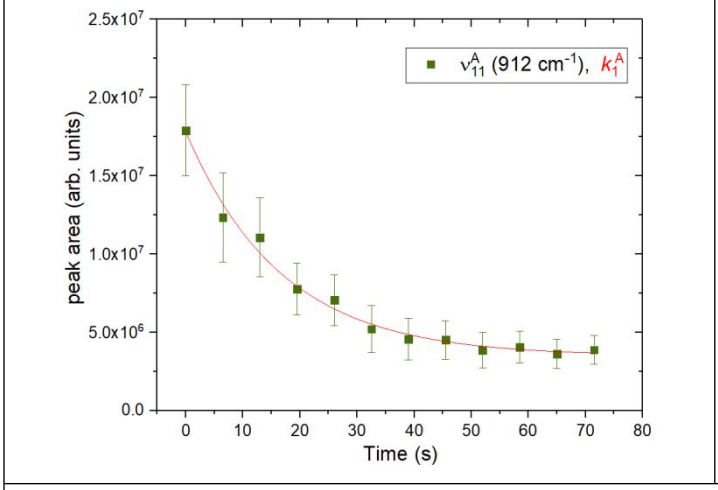

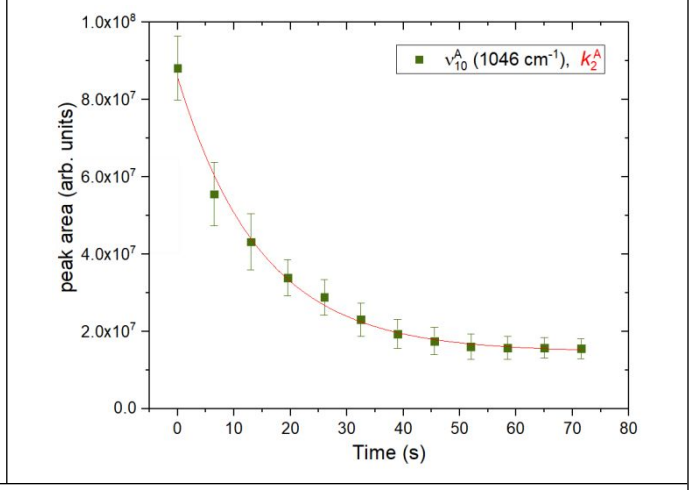

(B) Ionic liquid: anion bands

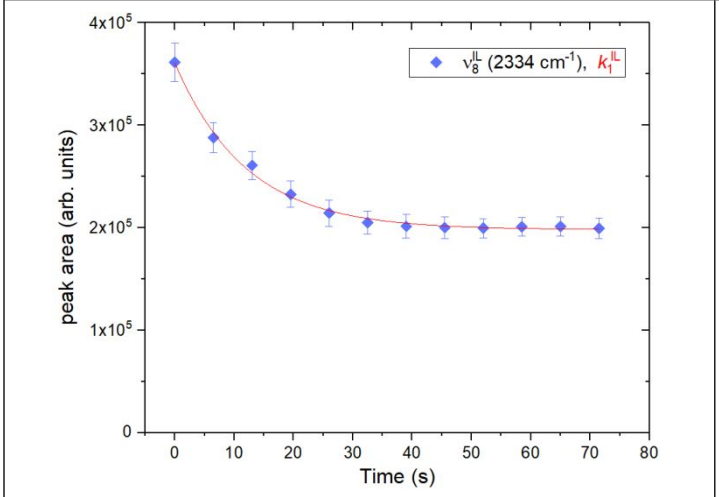

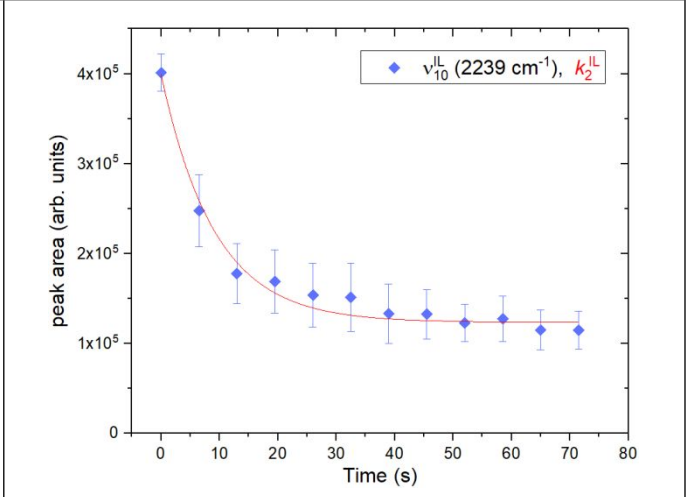

(C) Ionic liquid: cation bands

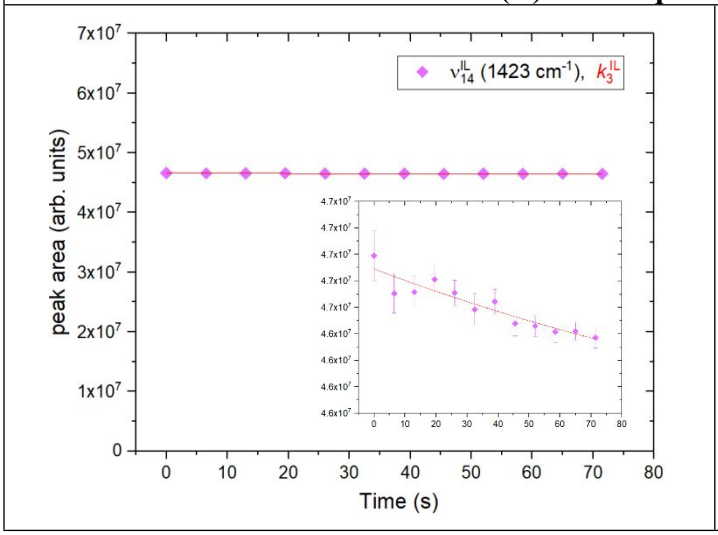

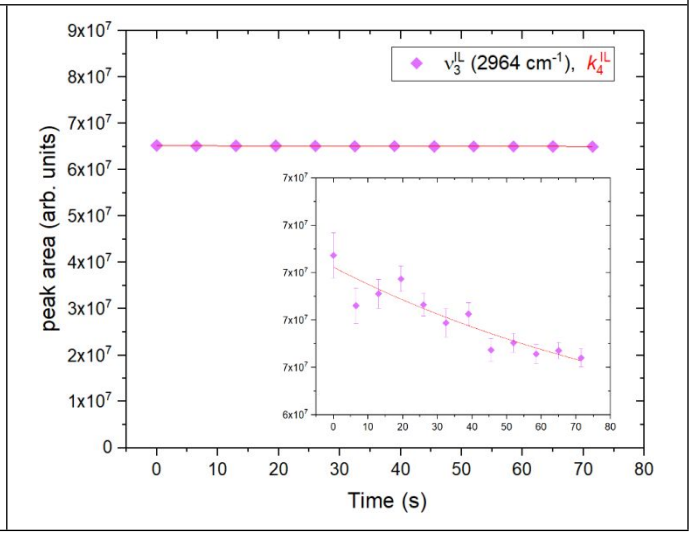

(ii) Products/intermediates

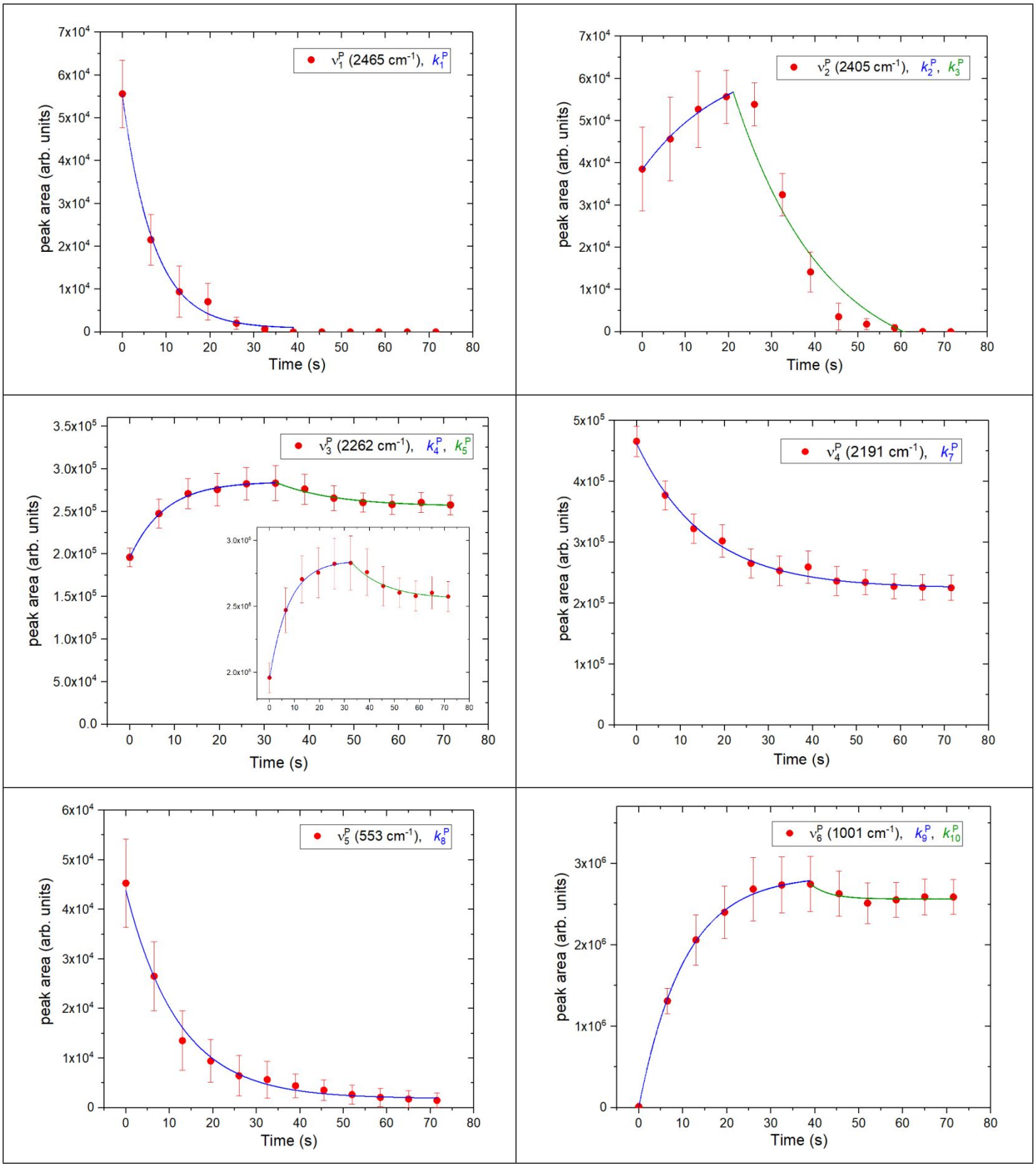

Figure 14. Temporal profiles for the select bands of the (i) reactants and (ii) products/intermediates

in the Raman spectra which arise due to chemical reaction for the merged droplet constituting the ionic liquid [EMIM][CBH] and aqueous solution of 30 % HNO_3.

Table 6: Rate constants evaluated from the alteration of Raman intensities of certain relevant bands/peaks for the reaction between the ionic liquid [EMIM][CBH] and HNO_3 solutions.

Species	Band	Wavenumber (cm^{-1})	Rate constant	Rate constant (s^{-1})		
				10 % HNO_3	20 % HNO_3	30 % HNO_3
HNO_3	ν_{11}^{A}	912	k_1^A	-	0.03 ± 0.01	0.06 ± 0.01
	ν_{10}^{A}	1046	k_2^A	0.010 ± 0.005	0.05 ± 0.01	0.07 ± 0.01
Mean rate constant (s^{-1})				0.010 ± 0.005	0.04 ± 0.01	0.07 ± 0.01
[CBH]	ν_{8}^{IL}	2334	k_1^{IL}	0.010 ± 0.001	0.05 ± 0.01	0.08 ± 0.01
	ν_{10}^{IL}	2239	k_2^{IL}	-	0.04 ± 0.01	0.11 ± 0.01
Mean rate constant (s^{-1})				0.010 ± 0.001	0.05 ± 0.01	0.10 ± 0.01
[EMIM]	ν_{14}^{IL}	1423	k_3^{IL}	0.003 ± 0.001	0.010 ± 0.005	0.005 ± 0.002
	ν_{3}^{IL}	2964	k_4^{IL}	0.003 ± 0.002	0.008 ± 0.004	0.009 ± 0.003
Mean rate constant (s^{-1})				0.003 ± 0.002	0.009 ± 0.005	0.007 ± 0.003
Products/ intermediates	ν_{1}^{P}	2465	k_1^P	-	-	0.14 ± 0.01
	ν_{2}^{P}	2405	k_2^P k_3^P	0.009 ± 0.002 -	0.04 ± 0.01 0.03 ± 0.01	0.05 ± 0.02 0.05 ± 0.02
	ν_{3}^{P}	2262	k_4^P k_5^P	0.009 ± 0.003 -	0.05 ± 0.01 0.04 ± 0.02	0.13 ± 0.01 0.08 ± 0.02
	ν_{4}^{P}	2191	k_6^P k_7^P	0.016 ± 0.005 -	0.05 ± 0.01 0.03 ± 0.01	- 0.06 ± 0.01
	ν_{5}^{P}	553	k_8^P	0.007 ± 0.002	0.03 ± 0.01	0.08 ± 0.01
	ν_{6}^{P}	1001	k_9^P k_{10}^P	-	-	0.13 ± 0.01 0.02 ± 0.01

3.5.3. Temporal profiles of products

The temporal patterns for the newly emerged bands attributed to products or intermediates are depicted in Figure 14. The peak intensity of the 2465 cm^{-1} (ν_1^P) band rapidly decreases with time; whereas the ν_2^P band at 2405 cm^{-1} shows an initial rise in the peak intensity followed by a sharp decay to zero. The time trace for ν_3^P band at 2262 cm^{-1} represents a less rapid growth followed by a shallow decay; and the ν_4^P band at 2191 cm^{-1} decays fast. The initial non-zero peak area values

for these bands reveal that these species could form instantaneously upon droplet merging. A rapid growth from zero peak intensity has been noted for the band at 1001 cm^{-1}, which undergoes a slow decay after 40 s since the merging event was initiated.

However, in case of 10 % HNO_3 merger (Figure S13), only a gradual growth has been noticed for the bands at 2405 (ν_2^P), 2262 (ν_3^P), and 2191 cm^{-1} (ν_4^P); this trend implies a continuing formation of these functional groups as the reaction progresses and the profiles could be replicated with a first-order growth mechanism through the rate law rise equation ($B = [A_0] (1 - e^{-kt})$) for an A → B reaction. In case of 20 % HNO_3, first a growth is observed, followed by a decay (Figure S12). Two possibilities can explain these finding. The newly evolved species are participating in a consecutive reaction to an unknown product. Alternatively, the products are gaseous and diffuse out the merged droplet effectively leading to decaying peak intensities. The latter scenario would gain support from continuous gas bubble formation as evident from the optical camera snapshots (Figure 7). Although the 553 cm^{-1} band (ν_5^P) still decays for all concentrations of HNO_3, these decays accelerate by a factor of 8 (20 %) and about 11 (30 %) compared to 10 %, as evident from the enhanced rate constants (Table 6). Therefore, we may conclude that the rapid formation of the RNCO functional group, which happens on a time scale faster than the time resolution of the collection of consecutive Raman spectra, and consecutive destruction is linked to the concentration of the HNO_3.

Quantitatively spoken, the sharp decay of k_1^P, which reflects the decrease of concentration of BH and/or BH_2 functional groups in the 30 % HNO_3 merger, and the absence at lower acid concentration suggest that the formation of this short-lived species is HNO_3 concentration dependent (0.14 s^{-1}). The rate constants for the production of B-H functional groups in -BH_3 group of mono-substituted borohydride or complexed BH_3 (k_2^P, k_4^P) for ν_2^P (2405 cm^{-1}) and ν_3^P (2262 cm^{-1}) and bridged BH_2 moieties (k_6^P) for ν_4^P (2191 cm^{-1}) in the 10 % HNO_3 merger were found to be smaller (0.009-0.016 s^{-1}) compared to the 20 and 30 % HNO_3 systems revealing rates in the range of 0.04-0.05 and 0.05-0.13 s^{-1}. For these three bands, first order exponential decays after the growth were noted, and the rate constants (k_3^P, k_5^P, k_7^P) were 0.03, 0.04 and 0.03 s^{-1}, respectively, for the 20 % HNO_3 merger. Once the HNO_3 concentration was raised to 30 %, the decay rate constants for these bands increased to 0.05, 0.08 and 0.06 s^{-1} indicating a faster loss mechanism.

3.6. Reaction mechanism

This manuscript would be incomplete without an assessment of our experimental findings in light of recent electronic structure calculations of the gas phase reaction of [EMIM][CBH] with HNO_3.[53] In such study, unsupervised critical point search was carried out at B3LYP/6-31G* level of theory and found thousands of relevant intermediates leading to the products detected here. Due to the large number of pathways, only the minimum energy paths connecting reactants to various products were ultimately used to justify the reaction mechanism. Since the motion of atoms are coupled in polyatomic molecules like those studied here, it is difficult to identify a "pure" normal mode that consist of only the moieties of interest (e.g., NC=O deformation, see Table 6). Therefore, normal modes were assigned by filtering on the basis of molecular connectivity (e.g., those having the moieties of interest) and those with sufficient normal mode displacements on the atoms of interest, finally, determining normal mode type (e.g., stretch, bend) through manual inspection. Overall, the reaction mechanisms of [EMIM][CBH] with HNO_3 have to account for the following key findings (**F1-F5**):

F1: In the merging process, temperature increases up to 435 K were monitored; this corresponds to molar enthalpy changes in the range of 3 to 10 kJ mol^{-1}. Therefore, reaction pathways involving significantly higher barriers are likely closed.

F2: Infrared spectroscopy revealed that hydrogen cyanide (HCN) and nitrous oxide (N_2O) were detected in all merging events with 10 % to 70 % HNO_3; nitrogen dioxide (NO_2) could only be observed in case of 70 % HNO_3. The nitrogen source in hydrogen cyanide (HCN) originated solely from the ionic liquid, while NO_2 commenced from HNO_3; two sources of N_2O were identified from [EMIM][CBH] (major route) and as the result of a reaction involving the aqueous medium (H_2O) (minor route). Quantitatively, individual branching ratios of HCN and N_2O up to 62 % were observed.

F3: As evident from the rate constants evaluated by Raman spectroscopy, $[CBH]^-$ is significantly more reactive compared to $[EMIM]^+$, with ratios of the reaction rates are 3 (10 %), 5 (20 %), and 14 (30 %) with the concentration of the acid provided in parenthesis. This finding can be correlated with finding **F2**, i.e. a significantly enhanced reactivity of the anion compared to the cation.

F4: The rate constants also reveal that the decay rates of the HNO_3 oxidizer and $[CBH]^-$ were essentially identical suggesting that the reaction of the oxidizer with the anion of the ionic liquid likely represents the initial step of the reaction.

F5: Raman spectroscopy revealed the emergence of products with key functional groups as the result of the merging process: B-H stretching and/or symmetric BH_2 stretching modes, B-H stretching of BH_3 corresponding to mono-substituted borohydride, B-H stretching of complexed BH_3, bridged BH_2 moieties, possibly the nitrosyl cation (NO^+), and -NCO functional groups. The decay rates of the latter accelerate significantly as the acid concentration increases.

These experimental findings place critical constraints on *possible* pathways provided in the computational study by accounting for **F1-F5** to identify likely *actual* pathway(s). *First*, pathways are restricted to reactions involving $[CBH]^-$ since both our experiments and the computations reveal a negligible reactivity of $[EMIM]^+$ (**F3**). *Second*, those computational pathways are searched for molecules carrying $BH/BH_2/BH_3$ and/or -NC=O functional groups, which match the Raman spectroscopically observed peak positions with an accuracy of ± 30 cm^{-1} (Table 6) (**F5**); this error range reflects potential red and blue shifts from the gas phase (calculated) to the condensed phase (experiment).[65] *Third*, we eliminate pathways leading to nitrogen monoxide (NO) from the ionic liquid. *Fourth*, pathways are restricted to those involving transition states not exceeding 30 kJ mol^{-1} with respect to the separated reactants; this reflects permissible pathways accounting for a maximum temperature increase of 435 K and, hence, molar enthalpy changes not exceeding 10 kJ mol^{-1} during droplet merging (**F1**) with about 11 % of the reactants in a 435 K Maxwell-Boltzmann distribution able to pass these transition states. Figures 15 and 16 compiles those intermediates, van-der-Waals complexes, products, and reaction pathways[53] fulfilling the aforementioned restrictions; interesting findings are revealed.

Distinct pathways from the reaction of $[CBH]^-$ with the HNO_3 oxidizer leading to HCN and N_2O are clearly identified and color coded in red and blue, respectively (**F2**). The reaction forming HCN is overall exoergic by 22 kJ mol^{-1} and commences from the reaction of the CBH^- anion and HNO_3 via a barrierless formation of the van-der-Waals complex **v1**, i.e. H_3B-C≡N…HNO_3. The latter isomerizes via hydrogen shift (**TS1**) from the carbon atom to boron yielding **v2** (H_3B-N≡C-H…NO_3^-) through a barrier residing 22 kJ mol^{-1} above the energy of the separated reactants. The HCN moiety is already present in this van-der-Waals complex. Hereafter, a nucleophilic substitution replaces HCN by the nitrate (NO_3^-) moiety trough the formation of a B-O bond and formation of **v3** (H_3BO-(NO_2)…HCN), which then reacts to the final products: HCN and the nitrato borohydride ion (H_3B-NO_3^-).

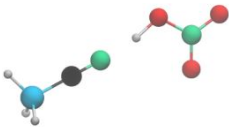

v1

vBH = 2202 cm^{-1}
vBH = 2317 cm^{-1}
vBH = 2341 cm^{-1}
vBH = 2344 cm^{-1}

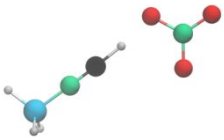

v2

vBH = 2350 cm^{-1}
vBH = 2386 cm^{-1}
vBH = 2390 cm^{-1}

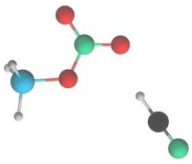

v3

vBH = 2335 cm^{-1}
vBH = 2365 cm^{-1}
vBH = 2373 cm^{-1}
vBH$_2$ = 987 cm^{-1}

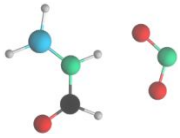

v4

vBH = 2491 cm^{-1}
vBH$_2$ = 985 cm^{-1}
vBH$_2$ = 1010 cm^{-1}

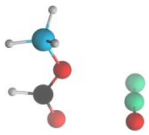

v5

vBH = 2281 cm^{-1}
vBH = 2288 cm^{-1}
vBH = 2370 cm^{-1}

v6

vBH = 2190 cm^{-1}
vBH = 2228 cm^{-1}
vBH = 2317 cm^{-1}
vBH$_2$ = 954 cm^{-1}

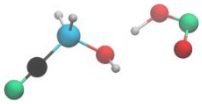

v7

vBH = 2207 cm^{-1}
vBH = 2313 cm^{-1}
vBH = 2316 cm^{-1}
vBH$_2$ = 953 cm^{-1}
vBH$_2$ = 1028 cm^{-1}

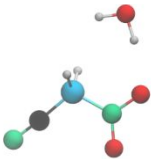

v8

vBH = 2389 cm^{-1}
vBH = 2413 cm^{-1}
vBH$_2$ = 980 cm^{-1}

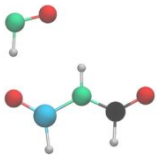

v9

vBH = 2288 cm^{-1}

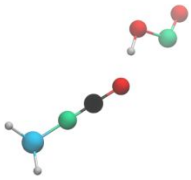

v10

vBH = 2285 cm^{-1}
vBH = 2315 cm^{-1}
vBH = 2316 cm^{-1}
vBH = 2357 cm^{-1}
vNCO = 525 cm^{-1}
vNCO = 543 cm^{-1}

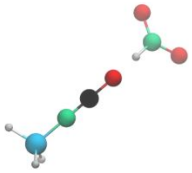

v11

vBH = 2286 cm^{-1}
vBH = 2315 cm^{-1}
vBH = 2317 cm^{-1}
vBH = 2357 cm^{-1}
vNCO = 524 cm^{-1}
vNCO = 545 cm^{-1}

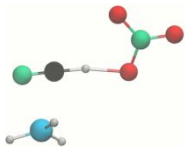

TS1

i1

vBH = 2218 cm^{-1}
vBH = 2281 cm^{-1}
vBH = 2281 cm^{-1}
vBH$_2$ = 950 cm^{-1}

i2

vBH = 2326 cm^{-1}
vBH = 2344 cm^{-1}
vBH = 2421 cm^{-1}
vBH$_2$ = 1023 cm^{-1}

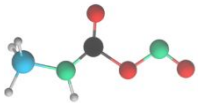

i3

vBH = 2285 cm^{-1}
vBH = 2308 cm^{-1}
vBH = 2313 cm^{-1}
vBH$_2$ = 951 cm^{-1}
vBH$_2$ = 998 cm^{-1}

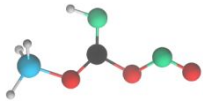

i4

vBH = 2271 cm^{-1}
vBH = 2282 cm^{-1}
vBH = 2349 cm^{-1}
vBH$_2$ = 986 cm^{-1}

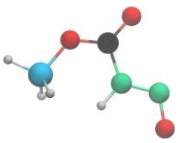

i5

vBH = 2312 cm^{-1}
vBH = 2333 cm^{-1}
vBH = 2337 cm^{-1}
vBH$_2$ = 974 cm^{-1}

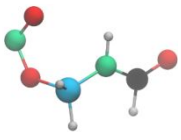

i6

vBH = 2344 cm^{-1}
vBH = 2369 cm^{-1}
vBH$_2$ = 971 cm^{-1}
vBH$_2$ = 1001 cm^{-1}
vBH$_2$ = 1037 cm^{-1}

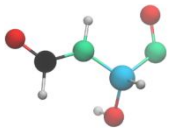

i7

vBH = 2119 cm^{-1}

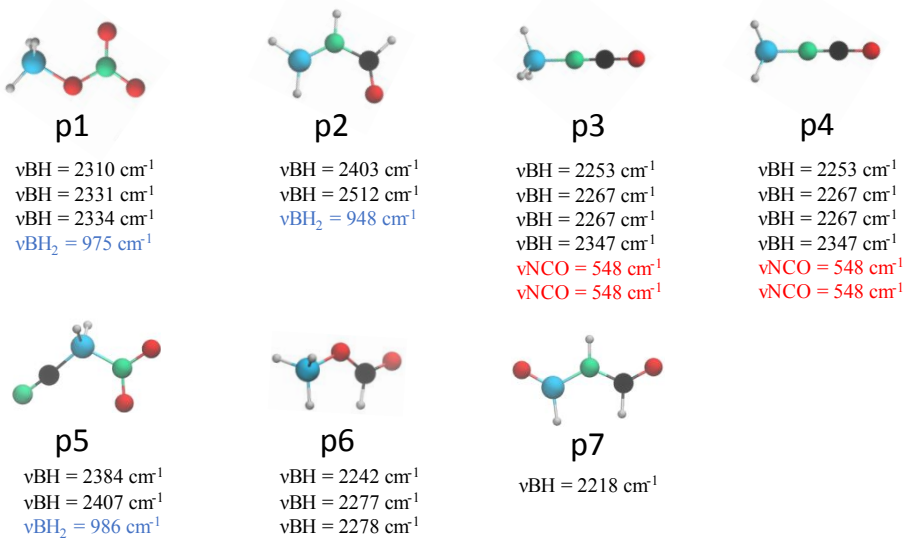

Figure 15. Reaction intermediates (i), van-der-Waals complexes (v), products (p) and their scaled vibrational modes matching within ± 30 cm^{-1} the Raman observations. The structure of initial proton transferred transition state (TS1) is also depicted here.

These van-der-Waals complexes also account for finding **F5**, i.e. B-H stretching (**v1, v2, v3**), symmetric BH_2 stretching modes (**v3**), and modes associated with BH_3 functional groups (**v1, v2, v3**). This pathway also confirms our experimental finding that the nitrogen atom of HCN originates from the ionic liquid, but not from the oxidizer (HNO_3) (**F2**). Further, the computational findings for the route **v1→v2** involving the acid and the anion can also be correlated with finding **F4**, i.e. identical decay rates of the HNO_3 oxidizer and $[CBH]^-$, signifying that the reaction of the oxidizer with the anion of the ionic liquid likely represent a dominating initial step of the reaction. The highest barrier in the **v1** → **v2** → **v3** → HCN + H_3B-NO_3^- pathway was predicted to be 22 kJ mol^{-1}; this implies that at a maximum energy release of about 10 kJ mol^{-1} upon mixing of the reactants (**F1**), 11 % of the reactant have sufficient energy to overcome the barrier to reaction. Considering the energy difference between hydrogen cyanide (HCN) and hydrogen isocyanide (HNC) of 62 kJ mol^{-1}, the formation of the HNC isomer would be endoergic by 40 kJ mol^{-1}, and only a fraction of 0.2 % of the reactants at most could overcome this endoergicity. The generation of the experimentally detected nitrous oxide (N_2O) could also start with the formation of a van-der-Waals complex (**v1**) between HNO_3 and $[CBH]^-$, which then undergoes proton transfer **v2** (H_3B-N≡C-H…NO_3^-) through a barrier of 22 kJ mol^{-1} above the separated reactants.

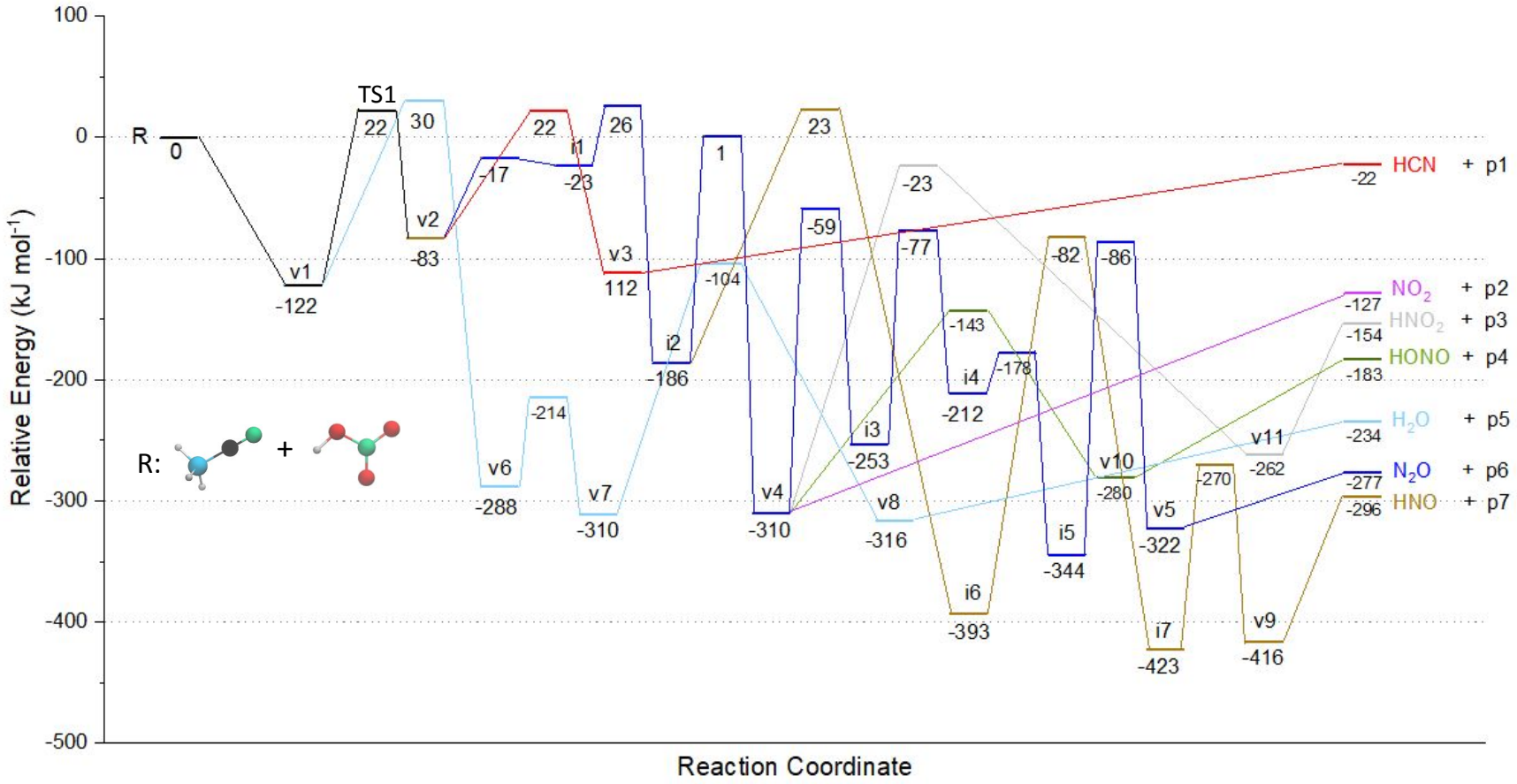

Figure 16. Potential energy surface of the gas phase reaction of the $[CBH]^-$ anion (H_3BCN^-) with nitric acid (HNO_3) adapted from Reference 53. Structures of the reaction intermediates (i), van-der-Waals complexes (v), and products (p) are compiled in Figure 15. Pathways to hydrogen cyanide (HCN) and nitrous oxide (N_2O) are clearly identified and color coded in red and blue, respectively.

A multistep reaction sequence **v2** → **i1**→ **i2** → **v4** → **i3** → **i4** → **i5** → **v5** involves formation of a carbon-oxygen bond [H_3B-N=CH-ONO_2^-; **v2** → **i1**], migration of the NO_2 moiety to the nitrogen atom [(O)HC-N(NO_2)(BH_3)$^-$; **i1**→ **i2**], hydrogen shift from the boron atom to the adjacent nitrogen atom accompanied by nitrogen-nitrogen single bond cleavage [(O)HC-NH=BH_2^-…NO_2; **i2** → **v4**], hydrogen migration from the carbon to the boron atom and simultaneous formation of a C-O bond [H_3B-NH-CO-ONO^-; **v4** → **i3**], migration of borane (BH_3) to the oxygen atom of the carbonyl moiety [H_3B-O-C(NH)(ONO)$^-$; **i3** → **i4**], NO group shift to form a N-N bond [H_3B-O-CO(HN)-N=O^-; **i4** → **i5**], hydrogen shift from the NH moiety to the carbon atom and simultaneous C-N cleavage [(O)HC-O-BH_3^-…N_2O; **i5** → **v5**] terminated by dissociation of the van-der-Waals complex to N_2O and the formyl borohydride anion [(O)HC -O-BH_3^-]. Note that the overall reaction to form these products from the reactants is highly exoergic by 277 kJ mol^{-1} with the highest transition state located 26 kJ mol^{-1} above the separated reactants to overcome in this reaction sequence. At a maximum energy release of about 10 kJ mol^{-1} upon mixing of the reactants (**F1**), 8 % of the reactants have sufficient energy to overcome the barrier to reaction. This fraction is 3 % lower than the path leading to HCN formation, suggesting that the formation of N_2O is less competitive as verified experimentally (**F2**). The van-der-Waals complexes and intermediates also reveal normal modes of B-H (**v1, v2, v4, v5, i1-i5**), BH_2 (**v4, i1-i5**), and BH_3 functional groups (**v2, v6, i1-i4**) as detected via Raman spectroscopy (**F5**).

Further, the Raman spectroscopic detection of NCO functional groups could be rationalized through the involvement of **v10** (H_2B-N=C=O^-…HONO) and/or **v11** (H_3B-N=C=O^-…HNO_2), which are linked to the formation of nitrous acid (HONO) and hydrogen nitryl (HNO_2), respectively (Figures 15 and 16). However, no evidence could be provided on the infrared spectroscopic detection of hydrogen nitryl (HNO_2). The pathway to **v11** would commence from **v4** through a barrier of 287 kJ mol^{-1}. The **v4** → **v11** pathway seems unlikely to compete with the **v4**→ **i3** reaction; this process has a barrier lowered by 36 kJ mol^{-1} and is involved in the formation of spectroscopically detected N_2O at mean branching ratios about 40 % compared to HCN, 60 %. Therefore, we may conclude that branching ratios and formation of hydrogen nitryl (HNO_2) – if any – is below the detection limit of our system providing upper limits of 2 % at most. Therefore, **v10** (H_2B-N=C=O^-…HONO) likely accounts for the spectroscopically observed isocyanate (NCO) functional group. **v10** can be accessed from **v4** via a low-energy barrier competing with those

required to eventually form N_2O. Consequently, **v10** should undergo decomposition to HONO and the dihydroboryl isocyanate ion (H_2B-N=C=O^-). A reanalysis of the experimental infrared data for the HIL – 70 % HNO_3 system (Figure 11) and subtraction of the HITRAN simulated gas phase spectrum of nitric acid (HNO_3) suggests that the most intense HON bending mode[66] for nitrous acid (HONO) at 1264 cm^{-1} could be tentatively assigned (Figure S14); recall, however, that based on the computed reaction path, formation of HONO is required to account for the detection of the isocyanate moiety (NCO) (**F5**). Further, we would like to reiterate that the experiments suggest that NO_2 originated in the HIL – 70 % HNO_3 system from the oxidizer; minor contributions from the decomposition of **v10** cannot be ruled out. Most important, the computed pathway to nitrosyl hydride (HNO) could not be confirmed experimentally. This route has to commence from isomerization of **i2** to **i6** via a transition state located 23 kJ mol^{-1} above the energy of the separated reactants; this pathway is less competitive compared to the isomerization of **i2** to **v4**, which has a barrier lowered by 22 kJ mol^{-1}. Therefore, **v9, i6**, and **i7** likely play no role in the reaction mechanism. Finally, the water elimination channel from **v1** cannot be confirmed nor denied experimentally since water represents the solvent of nitric acid (HNO_3).

4. Conclusions

Exploiting an ultrasonic levitation device in conjunction with a computational investigation, this work explored the reaction mechanisms and kinetics involved in the hypergolic reaction of droplets of 1-ethyl-3-methylimidazolium cyanoborohydride [EMIM][CBH] with droplets of nitric acid (HNO_3) at various concentrations from 10 % to 70 % at 300 K in an inert atmosphere of argon. The key experimental findings **F1** to **F5** can be rationalized via an initial proton transfer in the van-der-Waals complex **v1** between the oxidizer and the $[CBH]^-$ anion from the oxidizer to the anion of the ionic liquid accompanied by isomerization yielding **v2**. The van-der-Waals complex **v2** is central to the reaction mechanism and bifurcates the reaction pathways to eventually yield hydrogen cyanide (HCN) and nitrato borohydride ion (H_3B-NO_3^-) as well as nitrous oxide (N_2O) and formyl borohydride anion (HCO-O-BH_3^-) with dominating yields of hydrogen cyanide (HCN) compared to nitrous oxide (N_2O) (60 % versus 40 %). Although significant barriers of up to 22 kJ mol^{-1} with respect to the separated reactants were predicted computationally, experimentally determined heat released during the initial droplet merging event of up to 10 kJ mol^{-1} suggest that up to 11 % of the reactants could overcome the barrier to reaction. The rate constants provide

further experimental evidence that the $[CBH]^-$ anion is significantly more reactive compared to the $[EMIM]^+$ cation reaffirming the general consensus is that the hypergolicity of the HIL is determined by the anion of the ionic liquid.[25] The reaction intermediates, functional groups, and co-products involved in the hydrogen cyanide (HCN) and nitrous oxide (N_2O) routes also carry BH, BH_2, and BH_3 in substituted borohydride anion thus verifying the Raman spectroscopic detection of these functional groups. Based on the Raman spectroscopic detection of the isocyanate functional group (RNCO) in the van-der-Waals complex **v10** (H_2B-N=C=O^-…HONO)), nitrous acid (HONO) is also predicted to be a (minor) product; this species is obscured from a compelling infrared spectroscopic confirmation due to interferences from nitric acid (HNO_3).

A study of the [EMIM][CBH] - HNO_3 system could be expanded on multiple levels. So far, a computational study focused on the gas phase reactivity of the anion of the ionic liquid has been performed. The dominating role of the anion was certainly observed in the experiments, however, it cannot explain the distinct ignition delays by replacing the organic ethyl side group (5 ms) with butyl (BMIM; 11 ms), and allyl (AMIM; 600 ms) residues.[67] Therefore, the role of the cation – although less reactive than the anion with rates lower by about one order of magnitude – is critical to understand the ignition delay and hence to optimize the performance of engine systems. These studies shall be conducted experimentally and also computationally by including full solvent effects. Potential reactivity of the solvent was demonstrated to play a role in the formation of nitrous oxide (N_2O), where the oxygen originated from the solvent (here: water).

Conflicts of interest

There are no conflicts to declare.

Acknowledgements

This work was supported by the Air Force Office of Scientific Research (AFOSR) (FA9550-21-1-0377). The authors appreciate the Information Technology Service (ITS) from the University of Hawaii at Manoa for the computational resources.

References

1. Y. Zhang, H. Gao, Y. H. Joo and J. M. Shreeve, *Angew. Chem. Int. Ed.*, 2011, **50**, 9554-9662.
2. S. D. Chambreau, C. J. Koh, D. M. Popolan-Vaida, C. J. Gallegos, J. B. Hooper, D. Bedrov, G. L. Vaghjiani and S. R. Leone, *J. Phys. Chem. A*, 2016, **120**, 8011-8023.
3. A. R. Katritzky, J. W. Rogers, R. M. Witek, A. V. Vakulenko, P. P. Mohapatra, P. J. Steel and R. Damavarapu, *J. Energ. Mater.*, 2007, **25**, 79-109.
4. G. Reddy, J. Song, M. S. Mecchi and M. S. Johnson, *Mutat. Res.*, 2010, **700**, 26-31.
5. S. Wang, S. T. Thynell and A. Chowdhury, *Energy Fuels*, 2010, **24**, 5320-5330.
6. E. F. Rothgery, *Kirk-Othmer Encyclopedia of Chemical Technology*, 2004.
7. J. E. Troyan, *Ind. Eng. Chem.*, 1953, **45**, 2608-2612.
8. F. Cardulla, *J. Chem. Educ.*, 1983, **60**, 505-508.
9. J. Malm, *Eur. Chem. Agency*, 2013.
10. J. S. Broadley and J. M. Robertson, *Nature*, 1949, **164**, 915-915.
11. S. A. Forsyth, J. M. Pringle and D. R. MacFarlane, *Aust. J. Chem.*, 2004, **57**, 113-119.
12. S. Schneider, T. Hawkins, M. Rosander, G. Vaghjiani, S. Chambreau and G. Drake, *Energy Fuels*, 2008, **22**, 2871-2872.
13. Q. Zhang and J. M. Shreeve, *Chem. Rev.*, 2014, **114**, 10527-10574.
14. S. Schneider, T. Hawkins, M. Rosander, J. Mills, G. Vaghjiani and S. Chambreau, *Inorg. Chem.*, 2008, **47**, 6082-6089.
15. Q. Zhang, P. Yin, J. Zhang and J. M. Shreeve, *Chem.-Eur. J.*, 2014, **20**, 6909-6914.
16. H. Xue, Y. Gao, B. Twamley and J. n. M. Shreeve, *Inorg. Chem.*, 2005, **44**, 5068-5072.
17. Z. Zeng, B. Twamley and J. n. M. Shreeve, *Organometallics*, 2007, **26**, 1782-1787.
18. Z. Zhang, Z. Zhao, B. Wang and J. Zhang, *Green Energy Environ.*, 2021, **6**, 794-822.
19. S. Li, H. Gao and J. M. Shreeve, *Angew. Chem. Int. Ed.*, 2014, **53**, 2969-2972.
20. X. Zhang, W. Zhu, T. Wei, C. Zhang and H. Xiao, *J. Phys. Chem. C*, 2010, **114**, 13142-13152.
21. A. Chowdhury and S. T. Thynell, *Propellants, Explos., Pyrotech.*, 2010, **35**, 572-581.
22. C. Ye and J. n. M. Shreeve, *J. Chem. Eng. Data*, 2008, **53**, 520-524.
23. W. Xu, L.-M. Wang, R. A. Nieman and C. A. Angell, *J. Phys. Chem. B*, 2003, **107**, 11749-11756.
24. H. D. B. Jenkins, D. Tudela and L. Glasser, *Inorg. Chem.*, 2002, **41**, 2364-2367.
25. S. J. Brotton and R. I. Kaiser, *Anal. Chem.*, 2020, **92**, 8371-8377.
26. F. Lauck, J. Balkenhohl, M. Negri, D. Freudenmann and S. Schlechtriem, *Combust. Flame*, 2021, **226**, 87-97.
27. C. Sun and S. Tang, *Energy Fuels*, 2020, **34**, 2584-2589.
28. C. Sun and S. Tang, *Combust. Flame*, 2021, **228**, 107-113.
29. S. D. Chambreau, S. Schneider, M. Rosander, T. Hawkins, C. J. Gallegos, M. F. Pastewait and G. L. Vaghjiani, *J. Phys. Chem. A*, 2008, **112**, 7816-7824.
30. T. Litzinger and S. Iyer, *Energy Fuels*, 2010, **25**, 72-76.
31. K. Chingin, R. H. Perry, S. D. Chambreau, G. L. Vaghjiani and R. N. Zare, *Angew. Chem. Int. Ed.*, 2011, **50**, 8634-8637.
32. J. Xie and W. L. Hase, *Science*, 2016, **352**, 32-33.
33. J. Mikosch, S. Trippel, C. Eichhorn, R. Otto, U. Lourderaj, J. X. Zhang, W. L. Hase, M.

Weidemuller and R. Wester, *Science*, 2008, **319**, 183-186.
34. K. M. Vogelhuber, R. S. Booth and C. J. Annesley, *J. Phys. Chem. A*, 2018, **122**, 1954-1959.
35. M. R. Weismiller, C. E. Junkermeier, M. F. Russo, M. R. Salazar, D. Bedrov and A. C. T. van Duin, *Modell. Simul. Mater. Sci. Eng.*, 2015, **23**, 074007.
36. J. Liu, W. Zhou, S. D. Chambreau and G. L. Vaghjiani, *J. Phys. Chem. B*, 2019, **123**, 2956-2970.
37. J. Liu, W. Zhou, S. D. Chambreau and G. L. Vaghjiani, *J. Phys. Chem. B*, 2020, **124**, 4303-4325.
38. S. D. Chambreau, A. C. Schenk, A. J. Sheppard, G. R. Yandek, G. L. Vaghjiani, J. Maciejewski, C. J. Koh, A. Golan and S. R. Leone, *J. Phys. Chem. A*, 2014, **118**, 11119-11132.
39. J. Liu, S. D. Chambreau and G. L. Vaghjiani, *J. Phys. Chem. A*, 2014, **118**, 11133-11144.
40. W. Zhou, J. Liu, S. D. Chambreau and G. L. Vaghjiani, *J. Phys. Chem. B*, 2020, **124**, 11175-11188.
41. C. Carlin and M. S. Gordon, *J. Comput. Chem.*, 2015, **36**, 597-600.
42. R. Dorschner and G. Kaufmann, *Inorg. Chim. Acta*, 1977, **23**, 97-101.
43. G. H. Penner and A. R. Custodio, *Magn. Reson. Chem.*, 1994, **32**, 292-296.
44. S. J. Brotton and R. I. Kaiser, *Rev. Sci. Instrum.*, 2013, **84**, 055114.
45. S. J. Brotton, M. Lucas, S. D. Chambreau, G. L. Vaghjiani, J. Yu, S. L. Anderson and R. I. Kaiser, *J. Phys. Chem. Lett.*, 2017, **8**, 6053-6059.
46. S. J. Brotton, M. Lucas, T. N. Jensen, S. L. Anderson and R. I. Kaiser, *J. Phys. Chem. A*, 2018, **122**, 7351-7377.
47. S. J. Brotton and R. I. Kaiser, *J. Phys. Chem. A*, 2021, **125**, 2727-2742.
48. S. J. Brotton, M. J. Malek, S. L. Anderson and R. I. Kaiser, *Chem. Phys. Lett.*, 2020, **754**, 137679.
49. S. J. Brotton, S. D. Perera, A. Misra, N. F. Kleimeier, A. M. Turner, R. I. Kaiser, M. Palenik, M. T. Finn, A. Epshteyn, B. J. Sun, L. J. Zhang and A. H. H. Chang, *J. Phys. Chem. A*, 2022, **126**, 125-144.
50. M. Lucas, S. J. Brotton, A. Min, M. L. Pantoya and R. I. Kaiser, *J. Phys. Chem. Lett.*, 2019, **10**, 5756-5763.
51. M. Lucas, S. J. Brotton, A. Min, C. Woodruff, M. L. Pantoya and R. I. Kaiser, *J. Phys. Chem. A*, 2020, **124**, 1489-1507.
52. S. D. Perera, S. J. Brotton, H. Shinsato, R. I. Kaiser, Y. Choi and K. Na, *J. Phys. Chem. A*, 2021, **125**, 4896-4909.
53. K. Fujioka, R. I. Kaiser and R. Sun, *J. Phys. Chem. A*, 2023, **127**, 913-923.
54. S. J. Brotton and R. I. Kaiser, *J. Phys. Chem. A*, 2019, **123**, 1153-1167.
55. J. R. Berschied, Jr. and K. F. Purcell, *Inorg. Chem.*, 1970, **9**, 624-629.
56. S. A. Katsyuba, P. J. Dyson, E. E. Vandyukova, A. V. Chernova and A. Vidiš, *Helv. Chim. Acta*, 2004, **87**, 2556-2565.
57. S. A. Katsyuba, E. E. Zvereva, A. Vidiš and P. J. Dyson, *J. Phys. Chem. A*, 2007, **111**, 352-370.
58. T. Langner, A. Rietig and J. Acker, *J. Raman Spectrosc.*, 2020, **51**, 366-372.
59. N. Minogue, E. Riordan and J. R. Sodeau, *J. Phys. Chem. A*, 2003, **107**, 4436-4444.
60. D. M. Carey and G. M. Korenowski, *J. Chem. Phys.*, 1998, **108**, 2669-2675.
61. J. Kestin, M. Sokolov and W. A. Wakeham, *J. Phys. Chem. Ref. Data*, 1978, **7**, 941-948.

62. I. Isaac Sam, S. Gayathri, G. Santhosh, J. Cyriac and S. Reshmi, *J. Mol. Liq.*, 2022, **350**, 118217.
63. I. E. Gordon, L. S. Rothman, R. J. Hargreaves, R. Hashemi, E. V. Karlovets, F. M. Skinner, E. K. Conway, C. Hill, R. V. Kochanov, Y. Tan, P. Wcisło, A. A. Finenko, K. Nelson, P. F. Bernath, M. Birk, V. Boudon, A. Campargue, K. V. Chance, A. Coustenis, B. J. Drouin, J. M. Flaud, R. R. Gamache, J. T. Hodges, D. Jacquemart, E. J. Mlawer, A. V. Nikitin, V. I. Perevalov, M. Rotger, J. Tennyson, G. C. Toon, H. Tran, V. G. Tyuterev, E. M. Adkins, A. Baker, A. Barbe, E. Canè, A. G. Császár, A. Dudaryonok, O. Egorov, A. J. Fleisher, H. Fleurbaey, A. Foltynowicz, T. Furtenbacher, J. J. Harrison, J. M. Hartmann, V. M. Horneman, X. Huang, T. Karman, J. Karns, S. Kassi, I. Kleiner, V. Kofman, F. Kwabia–Tchana, N. N. Lavrentieva, T. J. Lee, D. A. Long, A. A. Lukashevskaya, O. M. Lyulin, V. Y. Makhnev, W. Matt, S. T. Massie, M. Melosso, S. N. Mikhailenko, D. Mondelain, H. S. P. Müller, O. V. Naumenko, A. Perrin, O. L. Polyansky, E. Raddaoui, P. L. Raston, Z. D. Reed, M. Rey, C. Richard, R. Tóbiás, I. Sadiek, D. W. Schwenke, E. Starikova, K. Sung, F. Tamassia, S. A. Tashkun, J. Vander Auwera, I. A. Vasilenko, A. A. Vigasin, G. L. Villanueva, B. Vispoel, G. Wagner, A. Yachmenev and S. N. Yurchenko, *J. Quant. Spectrosc. Radiat. Transf.*, 2022, **277**, 107949.
64. G. Socrates, *Infrared and Raman Characteristic Group Frequencies: Tables and Charts*, *Wiley***2004**.
65. B. Błasiak and M. Cho, *J. Chem. Phys.*, 2014, **140**, 164107.
66. R. H. Kagann and A. G. Maki, *J. Quant. Spectrosc. Radiat. Transf.*, 1983, **30**, 37-44.
67. S. C. Schneider, S. D.; Berman, M. *AFOSR Report.* **2014**, 17.